Reply to review 1

This paper describes an radar reflectivity operator and its adjoint for variational data assimilation. The new operator is implemented in WRFDA and preliminary test is presented with a convective case occurred in the U.S.. The developmental procedures of the operator is well described and the results are well explained and analyzed. My recommendation is to publish on GMD after minor revision. Although I do not have any major concerns about the content of the paper, I do suggest that the authors pay good attention to improve the English writing. Below are some suggestions from me to help improve the readability of the paper, but I strongly suggest the authors to hire a professional editor to further improve the paper.

We thank the reviewer for her careful review of our paper, and for her helpful comments that improved our paper. Our responses are given below in bold. RadZIceVar is renamed as RadarVar in the revision.

1. Title: The abbreviated algorithm name is not necessary in the title.

Fixed as reviewer's comment

2. Abstract, lines 15-18: Change to "It is shown that the deficiencies in the analysis using this operator, caused by the poor quality. . ..error covariance, can be partially resolved . . ..".

Fixed as reviewer's comment

3. Page 1, lines 24-25: ". . .Xue et al., 2006) and they have demonstrated that assimilating these observations improves. . ."

Fixed as reviewer's comment

4. Page 2, line 1: Change "limited in" to "limited to".

Fixed as reviewer's comment

5. Page 2, line 12: Add references for this statement.

Reference is added: "*Their expressions were derived according to the scattering amplitudes that were estimated through the T-matrix method and the Rayleigh scattering approximation (J08)*"

6. Page 2, line 13: Change "and the conditions that" to "in which".

Fixed as reviewer's comment

7. Page 2, line 22: Change this sentence to "Reflectivity operators have been developed both for the variational method (. . ..) and for the ensemble Kalman filter method. . .".

Fixed as reviewer's comment

8. Page 2, line 30: Suggested change: "Despite the difficulty, some efforts have been undertaken for reflectivity assimilation . . .."

Fixed as reviewer's comment

9. Page 3, line 14: "To compute Eq. (2), the mixing ratios of . . ... are required."

Fixed as reviewer's comment

10. Sections 2.1.2 and 2.1.3: There are so many parameters, such as those in Eqs. (11) and (16)-(20). Can you briefly explain the meanings of these parameters? Are they theoretically or empirically determined? What are their uncertainties?

For Eq. (11), most parameters are previously introduced (e.g., Γ, λ, π, $|Kw|^2$) or will be described in the following text. The value of the intercept parameter N_{0x} is given without any explanation, thus we add some words for this parameter (page 5, line 2-4).

"*The intercept parameters of these species are denoted by N_{0x}, the values of which are 3×10^6 m^{-4} and 4×10^5 m^{-4} for snow and graupel, respectively. Both values are consistent with the default values of ARPS EnKF where the J08 operator was implemented.*"

For Eq. (13), all parameters are duplications of J08. For readers not familiar with J08, we add some explanations for these parameters. For the standard deviation of canting angle, we add a reference to show its impact on differential reflectivity (page 5, line 10-12).

"*According to J08, $\bar{\phi}$ is zero for all hydrometeors, and σ is assumed to be different for snow (20°) and hail (60°). Here, we assume that σ for graupel is also 60°. The horizontal reflectivity that is concerned in this study is not sensitive to the canting angle (will be demonstrated in section 2.4), although the differential reflectivity is sensitive to canting angle (Aydin and Seliga, 1984).*"

For the backscattering amplitude associated parameters (α_{dxa} and α_{dxb}), we adopt the comment of reviewer 2 and recalculated these parameters using backscattering amplitude in pyCAPS (page 5, line 14-18).

**"*The coefficients of graupel are calculated using the backscattering amplitudes (for particle size <10 mm) in the pyCAPS-PRS v1.1 software (Dawson et al., 2014; Johnson et al., 2016; Jung et al., 2010; Jung et al., 2008) provided by the Center for Analysis and Prediction of*

***Storms (CAPS), and fitted to the polynomial function of f_{wg}. α_{dga} and α_{dgb} are the coefficients when f_{wg} is zero which means no rainwater.*"**

For Eqs. (16)-(20), all parameters are based on J08 except for the coefficients of graupel. Some variables are intermediate variables that are used to simplify the expression of J08. The derivation of these intermediate variables is shown in appendix. To make our statement clearer, we add some words in the related sentences (page 6, line 8-10).

"*where "x" is "s" (g) for snow (graupel), ε_x is 10^{-4} (10^{-3}) for snow (graupel), P_{wxak} and P_{wxbk} are precalculated constants for S-band radar, the value of n is 6, and the superscript k denotes the index of these constants. All these values are based on J08 except for those of graupel which are computed using the same method mentioned in 2.1.2.*"

(page 7, line 2) "*where P_{wxai} and P_{wxbi} are precalculated constants in Eq. (16) and are listed in Table 2.*"

11. Page 9, line 14: ". . .more substantially than that from dry snow. . ."

Fixed as reviewer's comment

12. Page 9, line 24: ". . ..from southern South Dakota to northern Nebraska, as shown in Fig.2. Note that there is also a weaker precipitation system near the north boundary of the domain. The top of the convective system of interest at this time, identified by reflectivity greater than 5 dBZ, reached 16 AGL". In the next line, "a bow echo was observed. . .". Line 3: delete "as shown in Fig. 2" here.

Fixed as reviewer's comment

13. Page 10, line 25: Change "that of snow and graupel" to "those of snow and graupel". Line 27: do you mean a broad vertical distribution?

Yes, a broad vertical distribution.

14. Page 11, line 25: "More outer loops were necessary due to the inaccurate . . .". Lines 26-28: do you mean a total of four experiments were performed by varying the number of iterations and the analysis time?

The experiments are Exp_ref and two of its variants. To make the statement clearer, we modify the related sentence to (page 12, line 17-19):

"*To determine the tradeoff between the analysis quality and computational cost, two variants of Exp_ref were conducted with 50 and 100 inner iterations. In each experiment, the radar DA analyses were performed at 00Z and 01Z.*"

15. Page 11, line 30: "RadZIceVar is unable to create hydrometeor increments. . ."?

Revised as "*Note that TL/AD of RadarVar will not be able to create reflectivity increments with the zero-hydrometeor background*"

16. Page 12, line 2: ". . .constant, it is expected that. . .". This should be a general expectation, so you do not have to refer to J08. Line 7: "nonzero" instead of "nonvanishing". Line 9: "To examine the analysis performance. . .". Line 14: add "the" before "length scale".

Fixed as reviewer's comment

17. Page 13, line 16: Why was such a small weighting 0.1 used? Did you tried any other weighting?

We have tried other weighting. In the case of using a larger weight coefficient, the impact of RadarVar will be weakened because the difference between the background and the observation becomes small. The initial cost function value with weighting 1.0 is 10 times smaller than that with weighting 0.1.

To make the statement clear, we add the following sentences
(page 12, line 31 – page 13, line 1)
"*In addition, current RadarVar cannot work with the weight coefficient of the retrieval part being smaller than 6×10^{-4} if the background contains no hydrometeor. A larger weight coefficient of the retrieval part (e.g., 0.5) reduces the difference between the background and the observation, which weakens the impact of direct DA using RadarVar and is contradictory to the purpose of this study.*"

18. Page 13, line 17: The use of "reflectivity space" and "model space" are not appropriate in this context. Also in line 5 on page 15. Line 18: delete "the" before "both". Line 20: delete "relatively".

The related words are is rewritten as "*in terms of the radar reflectivity and the mixing ratios of rain, snow, and graupel*" (page 14, line 12-13) and "*in terms of the radar reflectivity and hydrometeor mixing ratios*" (page 16, line 6)

19. Page 16, line 7: Suggest to replace "Two deficiencies are observed in the 3DVar analysis" by "Two problems of RadarVar were found in our test".

Fixed as reviewer's comment

For Review #2

This paper presents a forward operator, tangent linear model and its adjoint for reflectivity data assimilation (DA) in the variational framework. The procedures are very well documented in details, and the new systems are thoroughly evaluated. This manuscript could serve as a guideline for those who wish to develop tangent linear and adjoint models for new observation types. Although I believe this paper will make a valuable contribution to GMD, I have some concerns about the performance of the forward operator that need to be addressed. I have outlined my concerns below, and my overall recommendation is for acceptance pending major revisions.

We thank the reviewer for his/her careful review of our paper, and for his/her helpful comments that improved our paper. Our responses are given below in bold. RadZIceVar is renamed as RadarVar in the revision.

1. Some sentences are a bit confusing; for example, "A fixed N0r value is only available for a single-moment microphysics scheme." This could be rephrased to something like, "N0r values are typically fixed (or constant) in single-moment microphysics schemes." Other sentences could be revised to improve readability.

Fixed as reviewer's comments

2. Tables 1-2: The coefficients shown in Tables 1 and 2 were adopted from J08. In J08, they derived those coefficients for snow and hail. Therefore, the coefficients the authors adopted for graupel in this manuscript are indeed valid for hail and would result in reflectivity that is too high for graupel, which has a lower density than hail. Those coefficients should be replaced with coefficients for graupel.

Thanks for pointing out this.

Authors acknowledge that it is more proper to use graupel coefficients in this study. Therefore, we computed the graupel coefficients, fa(π) and fb(π), in the revision. These coefficients were computed using the backscatter amplitudes of graupel stored in pyCAPS software. In J08, the Rayleigh assumption was adopted for simplifying the equation and reducing the computational cost, but in pyCAPS, the backscatter amplitudes are computed using the T-matrix method and does not fully fit the Rayleigh assumption. However, for particle size smaller than 12 mm, the |fa|, as well as |fb| follows the relationship $|fa|=\alpha_{xa}D^{\beta xa}$ with a fixed α_{xa} and β_{xa} (=3.0) which is consistent with the assumption made in J08. This relationship is still approximately valid until the particle size is greater than 22 mm. J08 mentioned that the Rayleigh assumption resulted in reflectivity being overestimated for large particles; thus this drawback naturally exists in RadarVar. The following figure shows |fa| and |fb| as functions of f_w (water fraction).

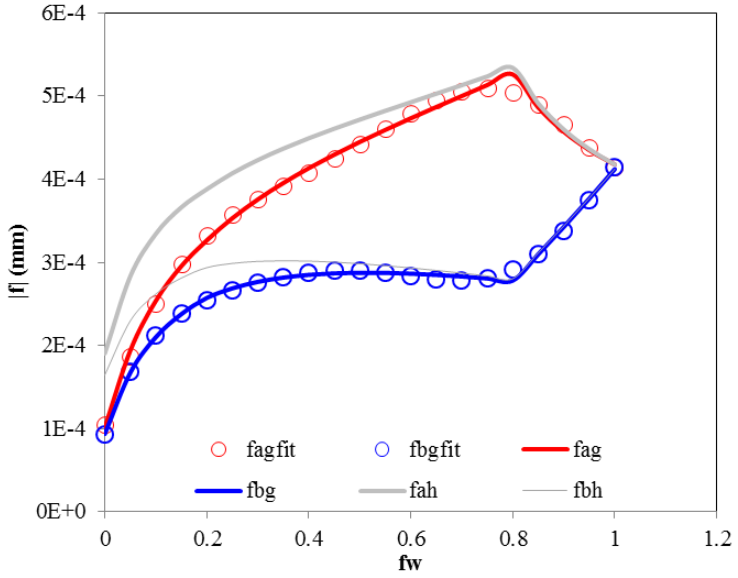

The backscatter amplitudes of hail are shown with gray solid lines; they are higher than their graupel counterparts (red for fa and blue for fb) as reviewer mentioned. Circles are fitting results using our graupel coefficients. These new coefficients are listed in Tables 1 and 2 in the revision.

All results except for those in section 4 (to be compared to the original J08 operator) are recalculated using the above graupel coefficients. The new results (scatter plots, cost functions, and the analysis reflectivity patterns) look similar to the previous results using hail coefficient except for some details.

3. Fig. 1b: It is hard to understand why the reflectivity for snow is much higher than the reflectivity for graupel. Because snow has a significantly lower density than graupel and the authors adopted hail coefficients for graupel, the reflectivity for graupel should be higher than the reflectivity for snow. Fig. 2 of J08 shows that backscattering amplitudes of hail as a function of the water fraction are larger than those of snow, which is opposite to Fig. 1b here.

It was our mistake when plotting this figure that wrong coefficients of hail phase (10 times smaller than the correct values) were used. Data in this plot has been updated in the revision.

4. Page 4, eq (5): Which value is used for the density of graupel? Is it 500 kg/m3 (typical value for graupel) or 913 kg/m3 (typical value for hail)?

The density of 400 kg m^{-3} was used. Meanwhile, the intercept parameter was also set to the value of graupel (4×10^5). Both values are obtained from ARPS EnKF where the original J08 operator was implemented.

To clarify the density value, we add *"where ρ_x is either the density of snow (100 kg m^{-3}) or graupel (400 kg m^{-3})"* at page 5, line 7.

5. Page 10, line 10: Why is the Thompson microphysics scheme used in this study? There are big differences between the snow and graupel size spectra assumptions used in the Thompson microphysics scheme and used in their DA system. This mismatch likely requires significant internal adjustments among state variables when the forecast model is launched after DA. For the purpose of evaluating the performance of their new system, it would make more sense to use a single-moment microphysics scheme that is consistent with their radar DA system.

Authors acknowledge that it would be better to use consistent MP parameters between the reflectivity operator in DA system and the microphysics scheme in model forecast. However, there is no improvement in terms of the forecast skill (FSS) and the initial RMSI difference between two cycles (00Z and 01Z) using a single-moment microphysics scheme (Goddard) with the density and intercept parameters being identical to RadarVar. For example, the initial RMSIs at 00Z and 01Z are 1.6×10^6 and 1.3×10^6 when Thompson scheme is used, while they are about 1.6×10^6 when the single moment scheme is used. With respect to the forecast skill, there is no improvement when the single-moment scheme is used.
Generally, it is not uncommon that DA system could use different assumptions from model. For example, scattering radiative transfer model for cloudy radiance DA does not always assume the same particle size distribution as WRF model's MP schemes. WRF has a lot of MP schemes, this radar operator was not designed specifically for Thompson scheme and we just use the Thompson scheme for the tests.

To make our statement clearer, we added the following sentence (page 10, line 21 – page 11, line 4):
"*Note that in current RadarVar implementation, the intercept parameters are fixed, while they spatiotemporally vary in the Thompson scheme. This inconsistent may increase the adjustment time for model initialization. However, this issue is secondary in the present because no improvement in terms of forecast skill which will be introduced was found in our early tests using a single-moment microphysics scheme with the density and intercept parameters being identical to RadarVar. The primary DA issue in this study is the poor background quality (due to no hydrometeor in GFS analysis or the precipitation displacement). The inconsistent between the operator and microphysics scheme will be considered in the future*"

6. Page 11, line 10: One dBZ observation error is too small, even if the performance does not change significantly with larger observation errors.

We reset the error to 2 dBZ, being consistent with J08 paper, and recalculated all results using this new observation error.

7. Page 11, line 19: The authors may use root-mean-square innovation (RMSI) instead of root-mean-square error (RMSE).

In data assimilation terminology, "innovation" is specifically referred to the background departure to observations and here we also talked about the analysis departure. So we changed to root-mean-square difference (RMSD).

8. Page 12, lines 19-24: The operator implemented in CAPS-PRS is not the operator presented in J08 but the one developed by Jung et al. (2010, JAMC), which uses the numerical integration of the T-matrix scattering amplitudes over the particle size distribution (PSD). This one includes the Mie effect as well. By default, CAPS-PRS would use the particle size distributions that are consistent with those used in the Thompson microphysics scheme. This means that the snow PSD is the combination of the gamma and exponential distributions, and the graupel PSD uses a diagnostic intercept parameter instead of a fixed value. Therefore, the almost exact fit between J08orig and RefZIceVar in Fig. 4 surprises me. I wonder if a mistake was made here.

Thanks for pointing this out.
Authors made a mistake in the statement; the results of the original J08 operator actually came from ARPS EnKF. We corrected the statement in the revision.

9. Page 13, lines 27-29: However, 0 dBZ observations are available in clear air. Are they not used to suppress spurious echoes?

Thanks for reviewer's comment.
In current implementation, the observed reflectivity not less than 0 dBZ data were used, while other data were assigned as missing data. The missing data are sometimes defined as non-precipitation echo, but how to define non-precipitation echo is still an open question. Some of studies define Z<5 dBZ as non-precipitation echo while some of other studies use threshold of -15 dBZ. We plan to add non-precipitation echo in future work.
Authors acknowledge this issue and add the following statement to note this issue (page 14, line 27-page 15, line 1).
"*Another cause of these spurious echoes is that non-precipitation echo was not assigned in the observation data in this study such that DA has no impact outside the observed convective area. Therefore, an approach to suppress the spurious echoes is to determine the non-precipitation points, assign a specific value like 0 dBZ to these points, and assimilate these non-precipitation echoes. The non-precipitation echoes will be considered in the future.*"

10. Fig. 14: Please add the line for thresholds for a skillful forecast and climatology.

Added as reviewer's comment.

A Radar Reflectivity Operator with Ice-Phase Hydrometeors for Variational Data Assimilation (~~RadZIceVar v1~~version 1.0) and Its Evaluation with Real Radar Data

Shizhang Wang[1,2], Zhiquan Liu[2]

[1]Collaborative Innovation Center on Forecast and Evaluation of Meteorological Disasters, Key Laboratory of Meteorological Disaster of Ministry of Education, Nanjing University of Information Science and Technology, Nanjing, 210044, China
[2] National Center of Atmospheric Research, Boulder, 80301, USA

Correspondence to: Zhiquan Liu (liuz@ucar.edu)

Abstract. A reflectivity forward operator and its associated tangent linear and adjoint operators (together named ~~RadZIceVar~~RadarVar) were developed for variational data assimilation (DA). ~~RadZIceVar~~RadarVar can analyze both rainwater and ice-phase species (snow and graupel) by directly assimilating radar reflectivity observations. The results of three-dimensional variational (3DVAR) DA experiments with a 3 km grid mesh setting of the Weather Research and Forecasting (WRF) model showed that ~~RadZIceVar~~RadarVar was effective at producing an analysis of reflectivity pattern and intensity similar to the observed data. Two to three outer loops with 50-100 iterations in each loop were needed to obtain a converged 3D analysis of reflectivity, rainwater, snow, and graupel, including the melting layers with mixed-phase hydrometeors. ~~The~~ It is shown that the deficiencies in the analysis using this operator ~~could be,~~ caused by the poor quality of the background fields and the use of the static background error covariance, ~~and these issues~~ can be partially resolved by using radar-retrieved hydrometeors in a preprocessing step and tuning the spatial correlation length scales of the background errors. The direct radar reflectivity assimilation using ~~RadZIceVar~~RadarVar also improved the short-term (2 h-5 h) precipitation forecasts compared to those of the experiment without DA.

1 Introduction

Over the past several decades, radar reflectivity observations have been used in many data assimilation (DA) studies (Borderies et al., 2018; Caumont et al., 2010; Gao and Stensrud, 2012; Hu et al., 2006; Jung et al., 2010; Jung et al., 2008; Liu et al., 2018; Putnam et al., 2014; Snook et al., 2012, 2015; Sun and Crook, 1997; Sun and Wang, 2013; Tong and Xue, 2005; Wang et al., 2013b; Wang and Wang, 2017; Wattrelot et al., 2014; Xiao et al., 2007; Xue et al., 2006) and they have demonstrated that assimilating this radar reflectivity improves the initial conditions of the convective scale and benefits the subsequent forecasts. To assimilate the reflectivity, it is necessary to transform the model's prognostic variables (e.g., rainwater, snow, and graupel) to the observed radar reflectivity. To perform this transformation, early studies (e.g., Sun and Crook, 1997; Xiao et al., 2007) used the Marshal–Palmer distribution of raindrop size (Z-R relationship). However, this

relationship is only valid in precipitation areas without ice-phase species; thus, its applications (e.g., Schwitalla and Wulfmeyer, 2018) are often limited ~~in~~to layers lower than 4 km or 8 km above ground level (AGL). To overcome this deficiency, more comprehensive operators that involve snow and graupel have been developed (Gao and Stensrud, 2012; Tong and Xue, 2005). Several studies (e.g., Gao and Stensrud, 2012; Wang and Wang, 2017) have demonstrated that involving these ice species in the reflectivity operator improves the analysis of hydrometeors in terms of their spatial distribution, especially in the vertical direction.

Although these operators have been successfully applied in many convective-scale DA studies, they were developed for a specific band of radar (e.g., S-band; Gao and Stensrud, 2012; Sun and Crook, 1997) and specific microphysics characteristics (e.g., with a fixed intercept parameter; Sun and Crook, 1997). However, mixed-phase species such as wet snow and wet graupel have not been considered in these operators. Recently, the contributions from mixed-phase species have been studied (Jung et al., ~~2008~~2008a, hereafter, J08; Posselt et al., 2015). To compute the mixed-phase species' contributions, J08 proposed an operator that was based on the expressions given by Zhang et al. (2001). Their expressions were derived according to the scattering amplitudes that were estimated through the T-matrix method and the Rayleigh scattering approximation~~.~~ (J08). For computational efficiency, these expressions were rewritten in the polynomial form that was only valid for S-band radar ~~and the conditions that~~in which the Rayleigh assumption was satisfied. Later, a more general and exact operator that fully used the T-matrix scattering method was proposed (Jung et al., 2010). This operator was given as the integral of the complex backscattering amplitudes over the size distribution of the precipitation particles (i.e., rainwater, snow, and graupel). In addition to these operators, several complex reflectivity operators in the integral form have also been proposed (Borderies et al., 2018; Caumont et al., 2006; Pfeifer et al., 2008; Ryzhkov et al., 2011; Wattrelot et al., 2014). Some were designed for a specific band of radar (e.g., W-band; Borderies et al., 2018), whereas some were designed for the bin microphysics scheme (e.g., Ryzhkov et al., 2011).

~~Currently, two approaches utilize these reflectivity~~Reflectivity operators~~. One is~~ have been developed both for the variational ~~DA~~ method (Caumont et al., 2010; Gao and Stensrud, 2012; Hu et al., 2006; Sun and Crook, 1997; Sun and Wang, 2013; Wang et al., 2013b; Wattrelot et al., 2014; Xiao et al., 2007~~),~~) and ~~the other is~~for the ensemble Kalman filter method (EnKF; Dawson et al., 2010; Jung et al., 2010; Jung et al., ~~2008~~2008a,b; Putnam et al., 2014; Snook et al., 2011, 2015; Tong and Xue, 2005; Xue et al., 2006). The variational method requires the tangent linear (TL) and adjoint (AD) operators, which are not required by the EnKF (Evensen, 2003). Therefore, complex operators such as those proposed by J08 are often employed in EnKF DA applications. For the variational method, a common approach to avoid using the TL/AD operators is to assimilate the reflectivity-retrieved hydrometeor profiles (Caumont et al., 2010; Wang et al., 2013a; Wattrelot et al., 2014); an alternative is to use the reflectivity as an additional control variable with the ensemble-variational DA approach (Wang and Wang, 2017).

Despite the difficulty, ~~many~~some efforts have ~~focused on~~been undertaken for reflectivity assimilation with the TL/AD operators (Gao and Stensrud, 2012; Kawabata et al., 2018; Liu et al., 2018; Xiao et al., 2007), and reasonable results have been obtained in terms of hydrometeor analysis and precipitation forecasts. However, none of these studies employed

operators as complex as those proposed by J08. Kawabata et al. (2018) adopted the expressions of Zhang et al. (2001) and developed the TL/AD operator for C-band radar but without taking into account the contributions from ice-phase species.

The main purpose of this study is to develop a TL/AD operator based on Jung et al. (2008) with the contributions of ice-phase precipitation and apply it in a variational DA framework. For convenience, the operator implemented in this study is called ~~RadZIceVar~~RadarVar to represent that it was developed for variational DA and contains ice-phase species. The original J08 operator is called J08orig. The reminder of this paper is organized as follows. In Section 2, the J08 operator is reviewed, and its TL and AD operators are derived. The experimental design is given in Section 3, and the new operators are verified in Section 4. The performance of ~~RadZIceVar~~RadarVar is discussed in Section 5, and the conclusions are presented in Section 6.

2 Reflectivity operator

2.1 Review of the J08 operator

The radar-observed reflectivity, Z, is given in logarithmic form as

$$Z = 10\log_{10} Z_e, \tag{1}$$

where Z_e is the equivalent reflectivity factor, which is the sum of the contributions from pure rainwater (Z_r), dry snow (Z_{ds}), dry graupel (Z_{dg}), wet snow (Z_{ws}), and wet graupel (Z_{wg}) as follows:

$$Z_e = Z_r + Z_{ds} + Z_{dg} + Z_{ws} + Z_{wg}. \tag{2}$$

To compute Eq. (2), ~~it is necessary to use~~ the mixing ratios of mixed-phase species (wet snow and wet graupel~~).~~) are required. However, many widely used microphysics schemes, such as the Lin, WSM6, and Morrison schemes, do not predict or diagnose the mixed-phase species; thus, the amount of rainwater in wet snow or graupel cannot be directly extracted from the model output. To solve this issue, J08 modeled the rain-snow (rain-graupel) mixture using a fraction that is given by

$$F = [\min(q_r / q_x, q_x / q_r)]^{0.3} F_{max}, \tag{3}$$

where F_{max} is the maximum fraction, which is 0.5 (0.3) for rain-graupel (rain-snow) mixtures; q_r is the mixing ratio of rainwater; and q_x is the general form of the mixing ratio of ice-phase species. The subscript "x" can be either "s" for snow or "g" for graupel. With this fraction, the mixing ratios of pure rainwater, dry snow, dry graupel and mixed-phase species are given by

$$\begin{aligned} q_{pr} &= (1 - F_{ws} - F_{wg}) q_r \\ q_{ds} &= (1 - F_{ws}) q_s \\ q_{dg} &= (1 - F_{wg}) q_g \\ q_{ws} &= F_{ws} (q_s + q_r) \\ q_{wg} &= F_{wg} (q_g + q_r) \end{aligned}, \tag{4}$$

where the subscripts "ws" and "wg" are added to F to represent the fractions of wet snow and wet graupel, respectively, and the subscripts "pr", "ds", and "dg" represent pure water, dry snow, and dry graupel, respectively. The mixed-phase density, ρ_{wx}, is not a constant and is parameterized by

$$\rho_{wx} = (1 - f_{wx}^2)\rho_x + f_{wx}^2 \rho_r \tag{5}$$

with

$$f_{wx} = \frac{q_r}{q_r + q_x}. \tag{6}$$

The subscript "x" in ρ_{wx}, ρ_x, and f_{wx} represents either snow (s) or graupel (g), and f_{wx} is called the water fraction.

2.1.1 Contribution from rainwater

In accordance with J08, all of the contributions are computed by integrations over the drop size distribution (DSD) weighted by the scatter cross section determined by the density, shape, and DSD. The DSD is modeled by an exponential distribution. After performing the integration, the contribution from pure rainwater, Z_r, is written in a simple form (Zhang et al., 2001; Posselt et al., 2015; Kawabata et al., 2018) as follows:

$$Z_r = \frac{4\lambda^4 \alpha_{ra}^2 N_{0r}}{\pi^4 |K_w|^2} \Lambda_r^{-(2\beta_{ra}+1)} \Gamma(2\beta_{ra}+1), \tag{7}$$

where λ is the wavelength of the radar, which is 107 mm for S-band radar, and N_{0r} is the intercept parameter of rainwater, which is 8×10^6 m^{-4} in this study. ~~A~~N_{0r} values are typically fixed ~~N_{0r} value is only available for a~~(or constant) in single~~-~~moment microphysics ~~scheme~~schemes; for a two-moment scheme, this value should be determined using the predicted number concentration. $|K_w|^2$ is the dielectric factor for rainwater and is equal to 0.93, and α_{ra} and β_{ra} are 4.28×10^{-4} and 3.04, respectively. The complete gamma function is written as $\Gamma(\ldots)$. The slope parameter of rain, Λ_r, is

$$\Lambda_r = \left(\frac{\pi \rho_r N_{0r}}{\rho_a q_{pr}}\right)^{\frac{1}{4}}, \tag{8}$$

where ρ_r =1000 kg m^{-3} is the rain density, q_{pr} is given by Eq. (4), and ρ_a is the density of air. By substituting Eq. (8) and the constant parameters into Eq. (7), we can rewrite Eq. (7) as a function of q_{pr} as follows:

$$Z_r(q_{pr}) = \mathrm{P}_r (q_{pr})^{1.77}, \tag{9}$$

where

$$\mathrm{P}_r = \frac{4\lambda^4 \alpha_{ra}^2}{\pi^4 |K_w|^2} \left(\frac{\pi \rho_r}{\rho_a}\right)^{-\frac{2\beta_{ra}+1}{4}} (N_{0r})^{1-\frac{2\beta_{ra}+1}{4}} \Gamma(2\beta_{ra}+1). \tag{10}$$

The value of P_r is approximately 4.8×10^9 with an air density of 1.0 kg m^{-3}. This value has the same magnitude as those proposed by Sun and Crook (1997) and Gao and Stensrud (2012).

2.1.2 Contribution from dry snow/graupel

The contributions from both dry and mixed-phase ice species after integration have the same form but differ in their coefficients. For dry ice species, the contribution is given by

$$Z_{dx} = \frac{4\Gamma(7)\lambda^4 N_{0x}}{\pi^4 |K_w|^2} \Lambda_{dx}^{-7} (A\alpha_{dxa}^2 + B\alpha_{dxb}^2 + 2C\alpha_{dxa}\alpha_{dxb}), \quad (11)$$

where the subscript *x* represents either snow (s) or graupel (g). The intercept parameters of these species are denoted by N_{0x}, the values of which are 3×10^6 m^{-4} and 4×10^5 m^{-4} for snow and graupel, respectively. Both values are consistent with the default values of ARPS EnKF where the J08 operator was implemented. The slope parameter in Eq. (11) for either dry snow or dry graupel is written as

$$\Lambda_{dx} = \left(\frac{\pi\rho_x N_{0x}}{\rho_a q_{dx}}\right)^{\frac{1}{4}}, \quad (12)$$

where ρ_x is either the density of snow (100 kg m^{-3}) or graupel (400 kg m^{-3}). The parameters *A*, *B*, and *C* in Eq. (11) are functions of the mean ($\bar{\phi}$) and the standard deviation (σ) of the canting angle and are given by

$$\begin{aligned} A &= \frac{1}{8}(3 + 4\cos 2\bar{\phi} e^{-2\sigma^2} + \cos 4\bar{\phi} e^{-8\sigma^2}) \\ B &= \frac{1}{8}(3 - 4\cos 2\bar{\phi} e^{-2\sigma^2} + \cos 4\bar{\phi} e^{-8\sigma^2}) \\ C &= \frac{1}{8}(1 - \cos 4\bar{\phi} e^{-8\sigma^2}) \end{aligned} \quad (13)$$

According to J08, $\bar{\phi}$ is zero for all hydrometeors, and σ ~~is different~~differs for snow (20 °) and hail (60 °). Here, we assume that σ for graupel is also 60 °. The horizontal reflectivity that is concerned in this study is not sensitive to the canting angle (will be demonstrated in section 2.4), although the differential reflectivity is sensitive to canting angle (Aydin and Seliga, 1984). In Eq. (11), ~~these functions~~*A*, *B*, and *C* are multiplied by coefficients (α_{dxa} and α_{dxb}) that describe the backscattering amplitudes. For dry ice-phase species, these coefficients are precalculated constants and are listed in Table 1. The coefficients of graupel are calculated using the backscattering amplitudes (for particle size <10 mm) in the pyCAPS-PRS v1.1 software (Dawson et al., 2014; Johnson et al., 2016; Jung et al., 2010; Jung et al., 2008) provided by the Center for Analysis and Prediction of Storms (CAPS), and fitted to the polynomial function of f_{wg}. α_{dga} and α_{dgb} are the coefficients when f_{wg} is zero which means no rainwater.

For brevity, Eq. (11) is rewritten as a function of q_{dx} for dry snow and dry graupel and is given by

$$Z_{dx}(q_{dx}) = P_{dx} q_{dx}^{1.75}, \quad (14)$$

where

$$P_{\mathrm{dx}} = \frac{4\Gamma(7)\lambda^4 N_{0\mathrm{x}}^{-0.75}}{\pi^4 |K_{\mathrm{w}}|^2} \left(\frac{\pi\rho_{\mathrm{x}}}{\rho_{\mathrm{a}}}\right)^{-1.75} (A\alpha_{\mathrm{dxa}}^2 + B\alpha_{\mathrm{dxb}}^2 + 2C\alpha_{\mathrm{dxa}}\alpha_{\mathrm{dxb}}) \cdot \quad (15)$$

2.1.3 Contribution from wet snow/graupel

The equation for the contribution from mixed-phase species has the same form as Eq. (11) except that the subscript "d" is replaced by "w" to represent wet species. The slope parameter for mixed-phase species also has the same form as Eq. (12) except that the subscript "d" is replaced by "w", and ρ_{wx} substitutes for ρ_{x}. For wet species, σ in A, B, and C is a function of f_{w} and q_{wg}. Additional details are given in Section 3c of J08. The coefficients that are multiplied by *A*, *B*, and *C* are functions of f_{w} and are written as

$$\begin{aligned} \alpha_{\mathrm{wxa}} &= \varepsilon_{\mathrm{x}} \sum_{k=0}^{n} P_{\mathrm{wxa}k} f_{wx}^{k} \\ \alpha_{\mathrm{wxb}} &= \varepsilon_{\mathrm{x}} \sum_{k=0}^{n} P_{\mathrm{wxb}k} f_{wx}^{k} \end{aligned}, \quad (16)$$

where "x" is "s" (*g*) for snow (graupel), ε_{x} is 10^{-4} (10^{-3}) for snow (graupel), $P_{\mathrm{wxa}k}$ and $P_{\mathrm{wxb}k}$ are precalculated constants for S-band radar, the value of *n* is 6, and the superscript *k* denotes the index of these constants. ~~Based~~All these values are based on J08~~, the value of *n* is 6.~~ except for those of graupel which are computed using the same method mentioned in 2.1.2. The values of $P_{\mathrm{wxa}k}$ and $P_{\mathrm{wxb}k}$ are listed in Table 2.

To simplify the derivation of the TL/AD operators, we rewrite Eq. (11) as a function of the mixed-phase mixing ratio (q_{wx}) and the water fraction (f_{w}) as follows:

$$Z_{\mathrm{wx}}(q_{\mathrm{wx}}, f_{\mathrm{wx}}) = P_{\mathrm{wx}} q_{\mathrm{wx}}^{1.75} \varepsilon_{\mathrm{x}}^2 \sum_{k=0}^{2n} P_{\mathrm{x}k} f_{\mathrm{wx}}^{k}, \quad (17)$$

where the coefficients P_{wx} and $P_{\mathrm{x}k}$ are given by

$$P_{\mathrm{wx}} = \frac{4\Gamma(7)\lambda^4 N_{0\mathrm{x}}^{-0.75}}{\pi^4 |K_{\mathrm{w}}|^2} \left(\frac{\pi\rho_{\mathrm{wx}}}{\rho_{\mathrm{a}}}\right)^{-1.75}, \quad (18)$$

and

$$P_{\mathrm{x}k} = AP_{\mathrm{Ax}k} + BP_{\mathrm{Bx}k} + 2CP_{\mathrm{Cx}k}, \quad (19)$$

respectively. $P_{\mathrm{Ax}k}$, $P_{\mathrm{Bx}k}$, and $P_{\mathrm{Cx}k}$ in Eq. (19) are given by

$$P_{\mathrm{A}xk}=\begin{cases}\sum_{i=0}^{k}P_{\mathrm{wx}ai}P_{\mathrm{wxa}(k-i)}, (k\le n)\\ \sum_{i=k-n}^{n}P_{\mathrm{wx}ai}P_{\mathrm{wxa}(k-i)}, (k>n)\end{cases}$$

$$P_{\mathrm{B}xk}=\begin{cases}\sum_{i=0}^{k}P_{\mathrm{wx}bi}P_{\mathrm{wxb}(k-i)}, (k\le n)\\ \sum_{i=k-n}^{n}P_{\mathrm{wx}bi}P_{\mathrm{wxb}(k-i)}, (k>n)\end{cases}, \quad (20)$$

$$P_{\mathrm{C}xk}=\begin{cases}\sum_{i=0}^{k}P_{\mathrm{wx}ai}P_{\mathrm{wxb}(k-i)}, (k\le n)\\ \sum_{i=k-n}^{n}P_{\mathrm{wx}ai}P_{\mathrm{wxb}(k-i)}, (k>n)\end{cases}$$

where $P_{\mathrm{wx}ai}$ and $P_{\mathrm{wx}bi}$ are precalculated constants in Eq. (16) and are listed in Table 2. The subscript "x" in these constant coefficients represents either snow (s) or graupel (g). The derivations of Eq. (17) to Eq. (20) are given in the appendix.

2.2 Tangent linear operator

Because ~~RadZIceVar~~RadarVar is highly nonlinear and complex, performing the derivation for every nonconstant variable in this operator is difficult. In addition, some components of ~~RadZIceVar~~RadarVar (e.g., the fraction F in Eq. (3)) are discontinuous and may cause serious convergence problems in the minimization (Janiskov á and Lopez, 2013; Janiskov á et al., 1999). Although this issue can be addressed by performing regularization for the discontinuous components in ~~RadZIceVar~~RadarVar, it is beyond the scope of this study. Here, we assumed that five variables in ~~RadZIceVar~~RadarVar are not changed in the minimization: i) the air density, ii) the fraction F, iii) the intercept parameter, iv) the standard deviation of the canting angle σ, and v) the density of the mixed-phase species. The air density is held constant for simplification and to focus on the impact of the changes in the hydrometeors. The fraction F is assumed to remain unchanged because of its second-order discontinuity at the point that q_x is equal to q_r. The intercept parameter is constant because ~~RadZIceVar~~RadarVar was currently designed for single-moment microphysics schemes. Although multimoment microphysics schemes are more realistic because they predict the number density of hydrometeors, single-moment microphysics schemes are still widely used to compute reflectivity and the polarization variables (e.g., Posselt et al., 2015). For simplification, the standard deviation of the canting angle and the density of the mixed-phase species remain unchanged in the minimization. These assumptions are discussed in Section 4.

2.2.1 Linearization for rain

Considering the assumptions presented above, P_r in Eq. (9) becomes a constant in the minimization. Therefore, the linearized form of Eq. (9) for q_{pr} is given by

$$\begin{aligned}\delta Z_r(q_{pr}) &= \frac{\partial Z_r(q_{pr})}{\partial q_{pr}}\frac{\partial q_{pr}}{\partial q_r}\delta q_r \\ &= 1.77\,P_r(q_{pr})^{0.77}(1-F_{ws}-F_{wg})\delta q_r\end{aligned} \quad . \tag{21}$$

2.2.2 Linearization for dry and wet snow/graupel

For dry snow and graupel, the linearized form of Eq. (14) is given by

$$\begin{aligned}\delta Z_{dx}(q_{dx}) &= \frac{\partial Z_{dx}}{\partial q_{dx}}\frac{\partial q_{dx}}{\partial q_x}\delta q_x \\ &= 1.75 P_{dx} q_{dx}^{0.75}(1-F_{wx})\delta q_x\end{aligned} \quad . \tag{22}$$

The linearization of Eq. (17) can be categorized into two parts, which represent the variations in Z_x caused by changes in q_{wx} and f_{wx}, respectively. The linear equation of Eq. (17) is written as

$$\begin{aligned}\delta Z_{wx}(q_{wx}, f_{wx}) &= \frac{\partial Z_{wx}}{\partial q_{wx}}\left(\frac{\partial q_{wx}}{\partial q_x}\delta q_x + \frac{\partial q_{wx}}{\partial q_r}\delta q_r\right) + \frac{\partial Z_{wx}}{\partial f_{wx}}\left(\frac{\partial f_{wx}}{\partial q_x}\delta q_x + \frac{\partial f_{wx}}{\partial q_r}\delta q_r\right) \\ &= \left(\frac{\partial Z_{wx}}{\partial q_{wx}}\frac{\partial q_{wx}}{\partial q_r} + \frac{\partial Z_{wx}}{\partial f_{wx}}\frac{\partial f_{wx}}{\partial q_r}\right)\delta q_r + \left(\frac{\partial Z_{wx}}{\partial q_{wx}}\frac{\partial q_{wx}}{\partial q_x} + \frac{\partial Z_{wx}}{\partial f_{wx}}\frac{\partial f_{wx}}{\partial q_r}\right)\delta q_x \\ &= \{1.75 P_{wx} q_{wx}^{0.75} F_{wx}\left(\varepsilon_x^2 \sum_{k=0}^{2n} P_{xk} f_{wx}^k\right) \\ &\quad + P_{wx} q_{wx}^{1.75}\left[\varepsilon_x^2 \sum_{k=0}^{2n} P_{xk} k f_{wx}^k \left(\frac{1}{q_r} - \frac{1}{q_r + q_x}\right)\right]\}\delta q_r \\ &\quad + \{1.75 P_{wx} q_{wx}^{0.75} F_{wx}\left(\varepsilon_x^2 \sum_{k=0}^{2n} P_{xk} f_{wx}^k\right) \\ &\quad + P_{wx} q_{wx}^{1.75}\left[\varepsilon_x^2 \sum_{k=0}^{2n} P_{xk} k f_{wx}^k \left(-\frac{1}{q_r + q_x}\right)\right]\}\delta q_x\end{aligned} \quad , \tag{23}$$

where the subscript "x" represents either snow (s) or graupel (g). Using s (g) to replace the subscript "x" in Eq. (23), we can obtain the tangent linear operator of the contribution from wet snow (wet graupel).

The linearization of Eq. (1) is given by

$$\delta Z = 10\frac{1}{Z_e \ln 10}\delta Z_e, \tag{24}$$

~~where δZ_e is the sum of δZ_r, δZ_{ds}, δZ_{dg}, δZ_{ws}, and δZ_{wg}.~~

where δZ_e is the sum of δZ_r, δZ_{ds}, δZ_{dg}, δZ_{ws}, and δZ_{wg}. Note that Z_e cannot be zero. Moreover, too small Z_e may result in an extremely large gradient during the minimization, which is undesirable. Therefore, the accepted minimum Z_e is set to 1.0 in current RadarVar. When the background value is smaller than this minimum value, DA system will discard the corresponding observation to prevent a large gradient. This minimum value can be smaller to ingest more observation and will be tuned in future work.

2.3 Adjoint operator

The adjoint operator is the transpose of the tangent linear operator. Because the tangent linear operator is applied to the model variables q_r, q_s, and q_g, the adjoint operator is written for these variables. First, the adjoint operator is written for Eq. (24). This operator has the following form:

$$\delta Z_e^{\mathrm{A}} = 10\frac{1}{Z_e \ln 10}\delta Z \ , \tag{25}$$

where the superscript "A" means adjoint.

For rainwater in Eq. (21), the adjoint operator is given by

$$\delta q_r^{\mathrm{A}} = \delta q_r^{\mathrm{A}} + 1.77\,\mathrm{P}_r (q_{pr})^{0.77}(1-F_{ws}-F_{wg})\delta Z_e^{\mathrm{A}}. \tag{26}$$

The parameter q_r^{A} on the right-hand side of Eq. (26) is the accumulated q_r^{A} before computing Eq. (26). This rule is also valid for q_x.

The adjoint operator of Eq. (22) is given by

$$\delta q_x^{\mathrm{A}} = \delta q_x^{\mathrm{A}} + 1.75 P_{dx} q_{dx}^{0.75}(1-F_{wx})\delta Z_e^{\mathrm{A}}. \tag{27}$$

Because Eq. (23) is the derivation with respect to both q_r and q_x, the adjoint operator of Eq. (23) contains two parts: one for rainwater and the other for ice species. For rainwater involved in Eq. (23), the adjoint operator is given by

$$\begin{aligned}\delta q_r^{\mathrm{A}} = {} & \delta q_r^{\mathrm{A}} + 1.75 P_{wx} q_{wx}^{0.75} F_{wx}(\varepsilon_x^2 \sum_{k=0}^{2n} P_{xk} f_{wx}^k)\delta Z_e^{\mathrm{A}} \\ & + P_{wx} q_{wx}^{1.75}[\varepsilon_x^2 \sum_{k=0}^{2n} P_{xk} k f_{wx}^k (\frac{1}{q_r} - \frac{1}{q_r+q_x})]\delta Z_e^{\mathrm{A}}\end{aligned}. \tag{28}$$

For ice species in Eq. (23), the adjoint operator is given by

$$\begin{aligned}\delta q_x^{\mathrm{A}} = {} & \delta q_x^{\mathrm{A}} + 1.75 P_{wx} q_{wx}^{0.75} F_{wx}(\varepsilon_x^2 \sum_{k=0}^{2n} P_{xk} f_{wx}^k)\delta Z_e^{\mathrm{A}} \\ & + P_{wx} q_{wx}^{1.75}[\varepsilon_x^2 \sum_{k=0}^{2n} P_{xk} k f_{wx}^k (-\frac{1}{q_r+q_x})]\delta Z_e^{\mathrm{A}}\end{aligned}. \tag{29}$$

2.4 Sensitivity of ~~RadZIceVar~~RadarVar to changes in hydrometeors

Since ~~RadZIceVar~~RadarVar is highly nonlinear, understanding its response to changes in q_r, q_s, and q_g assists in the analysis of DA results using this operator. The response functions for Eq. (9), Eq. (14), and Eq. (17) are plotted in Fig. 1. Figure 1b is a two-dimensional plot because Eq. (17) involves two kinds of hydrometeors. ~~Fig.~~Figure 1a shows that the reflectivity changes more rapidly for all three hydrometeors when the mixing ratios are less than 0.5 g kg^{-1}. As the mixing ratios increase to 2.0 g kg^{-1} or greater, the relationship between the reflectivity and the mixing ratio is approximately linear. This feature indicates that the reflectivity is more sensitive at small mixing ratios, and it also implies that the tangent linear approximation may give larger errors when the background reflectivity is small.

In addition, the reflectivity contribution from wet snow increases more substantially than that from dry snow when q_s or q_r are in the range of 0 – 0.5 g kg^{-1}. Fig. 1b shows that the reflectivity reaches 35 dBZ when both q_s and q_r are approximately 0.2 g kg^{-1}, while this reflectivity value requires q_s of ~1.2 g kg^{-1} for dry snow. This result is expected because many observation studies (e.g., Zhang et al., 2008) have shown that wet snow causes a bright band (large reflectivity) in the melting layer. This result also implies that the approximation error in the melting layer could be large.

3 Data and experimental design

3.1 Case review

This study focuses on a precipitation case that occurred in the northern U.S. The precipitation initiated at approximately 21Z on 1 June 2018, when convective cells formed near the border between South Dakota and Nebraska. By 00Z on 2 June 2018, these cells had developed into a linear convective system that was approximately 300 km long in the northeast-southwest direction and stretched from ~~the middle~~southern of South Dakota to ~~the middle of~~ northern Nebraska~~.~~, as shown in Fig. 2. Note that there is also a weaker precipitation system near the north boundary of the domain. The top of the convective system at this time ~~in terms of the observed~~, identified by reflectivity greater than 5 dBZ, reached 16 km AGL. This convective line developed further and moved to southeast Nebraska from 00Z to 04Z. During this period, a bow echo ~~could be~~was observed on the radar mosaic provided by the National Centers for Environmental Information (NCEI~~), as shown in Fig. 2.~~). By 08Z, the convective line had moved to the northern border of Kansas, followed by a large area of stratiform clouds that covered eastern Nebraska. The precipitation caused by this convective system lasted for nearly 20 h and ended at approximately 18Z on 2 June 2018.

3.2 Settings of the forecast model

Version 3.9.1 of the Weather Research and Forecasting (WRF; Skamarock et al., 2018) model was employed. All of the experiments were performed on a 450×450×42 domain centered at (41 °N, 96 °W) in eastern Nebraska (Fig. 2). The horizontal grid spacing was 3 km. The terrain-following vertical grid was employed with the model top at 50 hPa. All of the

experiments used the same physical parameterizations: no cumulus parameterization, the Thompson microphysics scheme (Thompson et al., 2004), the RRTMG longwave and shortwave radiation scheme (Iacono et al., 2008; Mlawer et al., 1997), and the Unified Noah land-surface model (Chen and Dudhia, 2001). Note that in current RadarVar implementation, the intercept parameters are fixed, while they spatiotemporally vary in the Thompson scheme. This inconsistent may increase the adjustment time for model initialization. However, this issue is secondary in the present work because no improvement in terms of forecast skill which will be introduced was found in our early tests using a single-moment microphysics scheme with the density and intercept parameters being identical to RadarVar. The primary DA issue in this study is the poor background quality (due to no hydrometeor in GFS analysis or the precipitation displacement). The inconsistent between the operator and microphysics scheme will be considered in the future. The initial conditions and the lateral boundary conditions were generated with the Global Forecast System (GFS) data at 00Z on 2 June 2018.

3.3 Generation of the background error covariance

~~RadZIceVar~~RadarVar was implemented in the WRF Data Assimilation (WRFDA) (Barker et al., 2012) system. To perform the variational DA with this newly developed radar operator, it is necessary to generate the background error covariance matrix with q_r, q_s, and q_g as part of the control variables. The generalized software package for the background error covariance statistics (GEN_BE) developed by Descombes et al. (2015) was used. The GEN_BE package can generate the univariate background error statistics for 11 variables, including these three hydrometeors. The background error statistics were computed using the National Meteorological Center (NMC) method (Parrish and Derber, 1992), which uses pairs of the differences between the 12 h and 24 h forecasts. A total of 27 days' forecasts from 20 May 2018 to 15 June 2018 were employed to generate the background error covariance.

The background error statistics for q_r, q_s, and q_g are shown in Fig. 3. The vertical distributions of the background error's standard deviation (Fig. 3a, b, c) are consistent with those of the corresponding hydrometeor profiles: the error of the rainwater mainly appears in the lower levels, while ~~that~~those of snow and graupel mainly ~~exists~~exist in the upper levels. The graupel may fall from the upper levels into the lower levels, so the graupel error has a broad vertical distribution. The horizontal correlation length scales of the background errors are often less than 4 grids (< 12 km), and the vertical correlation of each hydrometeor can be large at the associated precipitation levels. These spatial correlations of the hydrometeor errors determine the remote horizontal and vertical influences of the observed reflectivity.

3.4 Observation data and verification data

Radar data at 00Z and 01Z on 2 June 2018 were selected to evaluate the radar operator in a variational analysis framework because the convection was sufficiently deep to contain ice-phase species. To fully cover the convective system at 00Z, data from KABR, KFSD, KLNX, KOAX, KUDX, and KUEX were used, and KLNX was the closest radar from the convective line (Fig. 2). These radars were located in Nebraska and South Dakota. The radar data were stored in Level-II format and converted to WRFDA format using a modified 88D2ARPS package, which is widely used in radar DA studies (Putnam et al.,

2014; Snook et al., 2011, 2012). During this conversion, the radar data were also horizontally remapped to the model grids but remained at the radar elevations in the vertical direction; in other words, the horizontal resolution of the radar data after the conversion was consistent with that of the model. ~~Based on other studies (e.g., Umemoto~~To be consistent with the work using J08 operator (Jung et al., ~~2009~~2008b), the observation error of the reflectivity was set to ~~1~~2.0 dBZ. Our early tests using different observation errors indicated that the errors of the analysis reflectivity were comparable when using reflectivity errors ranging from 0.5 dBZ to 2.0 dBZ. For computational efficiency, we selected the remapped data every two grids in both the *x* and *y* directions for the DA.

The NCEP gridded stage IV (ST4) dataset (Lin and Mitchell, 2005) was used for the precipitation forecast verification. ST4 data with a horizontal resolution of 4 km were interpolated into the 3 km model grid mesh to evaluate the precipitation prediction. At each model grid, the interpolated value was the weighted average of the ST4 data within 10 km of the grid; these data were weighted by the square of the inverse of the distance between the model grid and the ST4 data location.

3.5 Experimental design

As the first attempt to implement and apply ~~RadZIceVar~~RadarVar in WRFDA, this study focused on the quality of the analysis using the univariate 3DVAR DA method in terms of the root-mean-square ~~error (RMSE~~difference (RMSD) against the observed reflectivity and the similarity between the observed reflectivity distributions and the analysis. The forecast performance is the secondary concern and will be explored more thoroughly in a future study with multivariate analysis using more advanced DA techniques.

All of the DA experiments analyzed only rainwater, snow, and graupel by assimilating only the radar reflectivity observations. The first DA experiment, called **Exp_ref**, is considered the benchmark experiment; it mostly used the default configurations of WRFDA-3DVAR, except the number of outer loops was set to six, and the number of maximum iterations in each outer loop was set to 150. More outer loops ~~is utilized~~were necessary due to ~~consider~~ inaccurate background hydrometeors and the high nonlinearity of the radar operator. To determine the tradeoff between the analysis quality and computational cost, two variants of Exp_ref were conducted with 50 and 100 inner iterations. ~~Two Exp_ref~~In each experiment, the radar DA analyses were performed at 00Z and 01Z ~~were performed~~. The background for the 00Z analysis was interpolated from the GFS analysis with zeros for the hydrometeor fields, and the background for the 01Z analysis was the 1-h WRF forecast from the 00Z analysis with more realistic hydrometeor fields.

Note that TL/AD of ~~RadZIceVar~~RadarVar will not be able to create ~~the change in~~ reflectivity ~~with hydrometeor perturbations~~increments with the zero-hydrometeor background (serves as the base state of TL/AD in the first outer loop), which is the case for the 00Z analysis. An approach to address this issue is to reset the zero background values of q_r, q_s, and q_g to small values that can range from 10^{-9} to 10^{-6} kg kg^{-1} (e.g., Wang and Wang, 2017). However, this approach will result in the fraction F being a constant, while ~~J08~~it is expected F to peak near the middle of the melting layer. Therefore, we introduced a hydrometeor preprocessing step before performing the analysis, which constructs a new background with the weighted sum of the radar-retrieved hydrometeor mixing ratios and their background counterparts. The hydrometeor

retrieval followed the procedure that is available in WRFDA, which is based on Gao and Stensrud (2012). The weight coefficients are arbitrarily set to 0.1 for the retrieval part and to 0.9 for the background. The small weight for the retrieval part was used to minimize the impact of the retrieval, mainly to ensure a ~~nonvanishing background.~~nonzero background. In addition, current RadarVar cannot work with the weight coefficient of the retrieval part being smaller than 6×10^{-4} if the background contains no hydrometeor. A larger weight coefficient of the retrieval part (e.g., 0.5) reduces the difference between the background and the observation, which weakens the impact of direct DA using RadarVar and is contradictory to the purpose of this study. The hydrometeor preprocessing was performed at both 00Z and 01Z in Exp_ref as a reference.

To ~~observe~~examine the analysis performance with a bad background, the Exp_ref analysis at 00Z was also run with a very small retrieval weight of ~~5~~6$\times10^{-4}$. In addition, the impact of the hydrometeor preprocessing on a relatively "good" background (01Z) was examined by comparing it with an experiment without hydrometeor preprocessing.

In several previous studies (Ban et al., 2017; Choi et al., 2017; e.g., Shen and Min, 2015), the horizontal correlation length scale factor of the background error had a large impact on the analysis. Therefore, two additional experiments, Exp_ls0.5 and Exp_ls0.125, were performed at 00Z with the length scale factors of 0.5 and 0.125, respectively.

Short-term forecasts from some of these analyses and from the GFS analysis (referred to as the 'noDA' experiment) were also carried out and evaluated.

4 Radar operator validation

Before evaluating the performance of ~~RadZIceVar~~RadarVar in WRFDA-3DVAR, we first examined the consistency between J08orig and ~~RadZIceVar. The pyCAPS PRS v1.1 software (Dawson et al.,~~ RadarVar. Because RadarVar follows the J08 operator, the operator implemented in ARPS EnKF (~~2014; Johnson et al., 2016; Jung et al., 2010;~~ Jung et al., 2008) ~~provided by the Center for Analysis and Prediction of Storms (CAPS)~~ was used to serve as the J08orig operator. To be comparable to J08orig operator, the coefficients of graupel listed in Tables 1 and 2, as well as the intercept parameter and hydrometeor density, are replaced by those listed in J08 which were designed for hail. These hail-associated coefficients are used only in section 4 for comparison. The noDA 4-hr forecast initialized at 00Z was used as the input of the radar operators. The results, which are shown in Fig. 4, indicate that the difference between J08orig and ~~RadZIceVar~~RadarVar is small and acceptable. The small difference is likely caused by the subtle programming differences between the two software packages.

To verify whether ~~RadZIceVar~~RadarVar is sensitive to the unchanged variables during the minimization (see Section 2b), four tests were conducted. The same noDA 4-hr forecast was used. In these tests, q_r, q_s, and q_g were randomly perturbed with standard deviations proportional to their input values; in other words, a large background mixing ratio caused a large perturbation. The tests called F_unprt, rhom_unprt, and SD_unprt represent that the fraction F, the mixed form density, and the standard deviation of canting angle, respectively, were unperturbed (i.e., fixed input calculated from the forecast input). The test called all_prt denotes that all of the variables in ~~RadZIceVar~~RadarVar were calculated using perturbed mixing ratios. The standard deviation of the perturbation was set to 10% of the background value; thus, the maximum perturbation could be

large, as shown in Fig. 5a. Fig. 5 shows that the reflectivities computed in F_unprt, rhom_unprt, and SD_unprt do not differ significantly from those computed in all_prt. This result indicates that keeping these variables unchanged during the minimization is an acceptable approximation. The most noticeable difference occurs in the middle layer, which is marked in red circles that plot off the diagonal line by several dBZ (Fig. 5c), but there are few of these samples.

The tangent linear operator of ~~RadZIceVar~~RadarVar was verified through a ratio, which is given by

$$\frac{\left|H(\mathbf{x}+\varepsilon\delta\mathbf{x})-H(\mathbf{x})\right|}{\varepsilon\left|\mathbf{H}(\delta\mathbf{x})\right|}=1+O(\varepsilon)\,, \tag{30}$$

where H and $\mathbf{H}$ represent the nonlinear operator and the corresponding TL version, respectively, $\mathbf{x}$ is the vector of the model state variables (q_r, q_s, q_g), whose perturbation is denoted by $\delta\mathbf{x}$, and ε is the perturbation magnitude and is greater than zero; $\delta\mathbf{x}$ used the perturbations generated for all_prt. Table 3 shows that the tangent linear operator is sufficiently accurate with a ratio close to 1.0.

A correct adjoint operator must satisfy the relationship that is given by

$$(\mathbf{H}\delta\mathbf{x})^{\mathrm{T}}\mathbf{H}\delta\mathbf{x}=\delta\mathbf{x}^{\mathrm{T}}\mathbf{H}^{\mathrm{T}}(\mathbf{H}\delta\mathbf{x})\,. \tag{31}$$

The meanings of all of the symbols in this equation are consistent with those in Eq. (30), and $\mathbf{H}^{\mathrm{T}}$ is the adjoint operator. All of the perturbations used for the tangent linear test were adopted in the adjoint test. In the double precision test, there were 14 identical digits on both sides of Eq. (31); in the single precision test, there were 7 identical digits.

5 Results

5.1 Analyses in the observation space and the model space

The Exp_ref analyses (6 outer loops, 150 inner iterations, and 0.1 weight for the retrieval part) are first examined in ~~both~~terms of the radar reflectivity ~~space~~ and ~~model space~~the mixing ratios of rain, snow, and graupel. As expected, the analyzed reflectivity agrees much more closely with the observed reflectivity than the background reflectivity for ~~the~~ both analysis times (00Z and 01Z) (Fig. 6). In addition, considering that the 00Z background bias is much larger than that at 01Z, the comparable analysis error for both times indicates that the analysis is generally relatively insensitive to the initial background. However, a small number of points in the analysis have zero reflectivity, while the corresponding observations can be greater than 10 dBZ (Fig. 6b, d). Further examination indicates that these failed points are related to the locations with very small background values of q_r, q_s, and q_g, where the nonlinearity of the radar operator and the deficiency of the TL/AD operator are more pronounced.

Figure 7 shows the horizontal distributions of the observed and analyzed reflectivities at 2 km, 4 km (melting layer), and 6 km AGL. In general, they match well in observed areas with a weaker analysis at 00Z, which is likely caused by the ~~relatively~~ bad background. Spurious echoes appear over unobserved areas in the analyses at both 00Z and 01Z and most likely resulted from the spatial correlations in the background error covariance; these correlations allow the propagation of

information from observed areas to unobserved areas both horizontally and vertically. This result implies that the statistical correlation length scales obtained from a one-month forecast sample may be too large for this squall line case. The results of tuning the horizontal correlation length scales will be given in Section 5.4. Another cause of these spurious echoes is that non-precipitation echoes were not assigned in the observation data in this study such that DA has no impact outside the observed convective area. An approach to suppress the spurious echoes is to determine the non-precipitation points, assign a specific value like 0 dBZ to these points, and assimilate these non-precipitation echoes. The non-precipitation echoes will be considered in the future.

The 00Z and 01Z analyses of q_r, q_s, and q_g at three model levels are shown in Fig. 8. The direct assimilation of the reflectivity data using ~~RadZIceVar~~RadarVar successfully retrieved the lower level rain, the upper level snow or graupel, and mixed rain/snow and/or rain/graupel in the melting layer (model level 15). Note that the analysis increment can be created only at levels where the STD of the background error is larger than zero (see Fig. 3).

5.2 Convergence of the minimization

Figure 9 shows the cost function and the norm of its gradient as a function of the number of inner iterations for the 1st, 3rd, and 6th outer loops. For the 00Z Exp_ref analysis, both the cost function and the gradient norm decrease rapidly in the first outer loop due to the large adjustment from the bad initial background. Using the improved guess after 2 outer loops, the third outer loop starts from an ~85% smaller cost function, which is then reduced more gradually with increasing iterations. Performing more outer loops does not further reduce the cost function substantially, and outer loop 6 even has a slightly larger cost function than that of outer loop 3. Similar behavior can also be observed in the 01Z analysis, but performing more than three outer loops can further reduce the cost function to a small extent. This indicates that performing six outer loops may not be necessary and that 2 or 3 outer loops may be sufficient.

To more quantitatively measure the impacts of the number of outer loops and inner iterations, the correlation coefficients between the Exp_ref analysis (i.e., 6 outer loops and 150 iterations in each loop) and the analyses with 1-5 outer loops and 50/100/150 inner iterations in each loop are calculated and shown in Fig. 10. In the 00Z analysis, the correlation coefficients of q_r and ~~q_s~~q_g are already greater than 0.~~8~~9 after the first outer loop, and using 50 or 100 inner iterations also results in good agreement with the Exp_ref analysis for q_r and ~~q_s~~q_g. However, this is not the case for ~~q_g~~q_s, which is likely an indication of a bad ~~q_g~~q_s background (0.1 of the retrieved values). ~~With~~ Given that the correlation coefficients of reflectivity reaches 0.9 after the second outer loop, the low correlation coefficients of q_s also implies that it is difficult to distinguish the contributions from ice-phase species. Even with a more realistic background at 01Z, the issue of the ~~q_g~~q_s analysis ~~is not pronounced~~ with less iterations and outer loops (Fig. 10b~~), and the~~) still exists, but the higher correlation coefficient of the run with 150-iteration after 4 outer loops, compared to the counterparts in the 00Z analysis~~ with three outer loops and 100 inner iterations in each loop gives coefficients greater than 0.8 for both q_r and q_s, further confirming,~~ indicates the importance of the background quality. Note that the hydrometeor's phase information could be better determined by assimilating polarization measurements from dual-polarization radar, which will be explored in a future study.

5.3 Importance of hydrometeor preprocessing

To further investigate the sensitivity of the analysis to the background quality, additional analyses without the hydrometeor preprocessing step were performed at 00Z and 01Z. At 00Z, the nonzero background was constructed by using a very small weight (~~5~~7 ×10^{-4}) for the retrievals. At 01Z, the background is simply taken from the 1-h WRF forecast. Compared to Fig. 6b, the analysis at 00Z (Fig. 11b) has many more failed points (i.e., those with zero analyzed reflectivity) due to the excessively small background hydrometeor values. In contrast, the 01Z analysis (Fig. 11d) without preprocessing has a comparable error bias and STD to those with the preprocessing (Fig. 6d). These results indicate that the preprocessing step is mostly needed to address the bad background.

~~Fig.~~Figure 12a shows that the analyzed reflectivity in the melting layer has a reasonable fit to the observations even though it started from very small values of the background reflectivity. ~~However, the~~The analysis in the model space (Fig. 12b) is ~~very different from~~also similar to that with the preprocessing (Fig. 8b). ~~With~~However, the reflectivity coverage (>35 dBZ) in Fig. 12a is smaller than those in the ~~preprocessing step, the analyzed melting layer is mostly a mixture of rainwater~~observation and ~~snow, while a three-phase mixture of hydrometeors is present when no preprocessing is applied. Note that the hydrometeor's phase information could be better determined by assimilating polarization measurements from dual-polarization radar~~Exp ref, which ~~will be explored in a future study.~~ corresponds to the horizontally distributed points on the bottom of Fig. 11b. In contrast, the 01Z analysis without the preprocessing step (Fig. 12c, d) closely resembles that with the preprocessing (Fig. 7h and Fig. 8e) in ~~both~~terms of the ~~observation~~radar reflectivity and ~~model spaces~~hydrometeor mixing ratios, especially over the strong convective line (black dashed line in Fig. 12d). However, removing this preprocessing step results in a large spurious ~~strong~~ echo (marked by "A" in Fig. 12c) that is ~~much weaker~~smaller in Fig. 7h. This implies that the preprocessing step will still be helpful for some "bad" locations (e.g., mismatched convective cells between the model background and observation) for a generally "good" background.

5.4 Impact of the spatial correlation scale

Figure 13 shows the 00Z analysis reflectivity at 4 km AGL with the horizontal correlation length scales of the background errors reduced by factors of 2 and 4. The spurious echoes weaken as the length scale decreases, especially for the ~~strong~~ spurious ~~echo~~echoes marked by "A". In addition, reducing the length scale improves the intensity analysis at certain locations (e.g., the convective cell marked by "B"; also see Fig. 7e, 7f). Note that the background error statistics used for these 3DVAR analyses were obtained from forecast samples over a month-long period and are likely not optimal for this particular squall line case. A better solution would be the use of the flow-dependent background error covariance, which will be investigated in the future using more advanced DA methods, such as 4DVAR and hybrid-3D/4DEnVar that are available in WRFDA.

5.5 Impact on the precipitation forecast

The performances of the precipitation forecasts were quantitatively evaluated using the Stage IV dataset with the fractions skill score (FSS; Roberts and Lean, 2008). Hourly precipitation forecasts between 02Z and 05Z were evaluated because assimilating only the reflectivity is expected to have an impact mostly on the short-term forecast. Similar to Schwartz et al. (2014), the aggregated FSS over the period from 02Z to 05Z is shown in Fig. 14 for the forecasts initialized at 00Z and 01Z and for different rainfall thresholds. For the forecast from 00Z (Fig. 15a), Exp_ref obtained greater FSSs than those of noDA for ~~all~~ thresholds greater than 5 mm h^{-1} with a radius of influence smaller than ~~50~~40 km. With a larger radius, this difference remains for the ~~light~~lighter rain (~~≤ 5~~(<20 mm h^{-1}) but disappears for the ~~heavier~~heavy rain~~.~~ (≥20 mm h^{-1}). Similar behavior can be observed for the forecast at 01Z (Fig. 15b) but with a more positive impact from the radar DA for heavier rainfall and for a radius of influence ~~greater~~smaller than 50 km. Further examination (not shown) indicated that the improvement in the ~~light~~moderate rain (>5mm h^{-1}) prediction was associated with the larger snow area in the analysis, so the light rain missed by noDA was better captured in Exp_ref. This examination also showed that the higher FSSs obtained by Exp_ref for the heavier rainfall were mostly associated with the smaller displacement error.

6 Conclusions

This study developed tangent linear and adjoint operators based on the J08 reflectivity operator and implemented them in WRFDA. This new operator can compute the reflectivity contributed by ice-phase species and is called ~~RadZIceVar.~~ ~~RadZIceVar~~RadarVar. RadarVar is effective at analyzing rainwater, snow, and graupel by directly assimilating US WSR-88D S-band radar reflectivity with WRFDA's 3DVAR. The analysis accuracy is somewhat sensitive to the numbers of outer loops and inner iterations. The results indicated that 2-3 outer loops with 50-100 iterations in each loop are needed to obtain a sufficiently accurate analysis. Two ~~deficiencies are observed~~problems of RadarVar were found in ~~the 3DVAR analysis~~our test. One issue is the analysis failures at locations with observed radar echoes but with zero or excessively small model background values of the hydrometeors. This issue can be partially resolved using a preprocessing step with radar-retrieved hydrometeors to improve the "bad" background before the analysis. Another issue is the spurious radar echoes (i.e., precipitation) in the analysis caused by the spatial correlations in the background error covariance. These can be reduced by decreasing the correlation length scales. In addition, the short-term (2 h – 5 h) precipitation forecast is improved by the direct reflectivity DA even though the inexpensive univariate 3DVAR technique is used in this first attempt of applying ~~RadZIceVar~~RadarVar.

A more thorough evaluation of reflectivity DA with ~~RadZIceVar~~RadarVar will be examined in a future study using a more advanced hybrid ensemble-variational DA technique, which allows flow-dependent background errors with multivariate correlations and is expected to further reduce the aforementioned deficiencies. Moreover, ~~RadZIceVar~~RadarVar will be extended to include the computation of polarimetric quantities to better determine the phases of the hydrometeors, especially in the melting layers.

Code and data availability

The ~~RadZIceVar~~RadarVar v1.0 operator is integrated into the community WRFDA software and will be publicly available in a future release. ~~The data used in this study can be obtained by contacting the corresponding author via e-mail.~~The code of RadarVar v1.0 and the scripts for running experiments in this study can be obtained at https://github.com/children1985/WRFDA_gmdd. The GFS data are available at https://www.ncdc.noaa.gov/data-access/model-data/model-datasets/global-forcast-system-gfs and the radar data can be downloaded at https://www.ncdc.noaa.gov/nexradinv/.

Author contributions

Shizhang Wang performed the coding and designed the data assimilation experiments. Zhiquan Liu supervised this study. All authors contributed to the writing of the paper.

Acknowledgements

This work was jointly sponsored by the National Key Research and Development Program of China (2017YFC1502103), the National Natural Science Foundation of China (41505089, 41875129, 41505090, 41430427, and 41805070), the Startup Foundation for Introducing Talent of NUIST (2014R007), and National Key Research and Development Program of China (2018YFC1506404）. NCAR is sponsored by the US National Science Foundation.

Appendix

This section provides details about the reorganization of all of the terms in the brackets in Eq. (11) in terms of the f_{wx} power. For convenience, the expressions in these brackets are represented by G(f_{wx}).

Applying Eq. (16) to the brackets in Eq. (11) results in

$$G(f_{wx}) = \varepsilon_x^2[A(\sum_{k=0}^{n} P_{wxak} f_{wx}^k)^2 + B(\sum_{k=0}^{n} P_{wxbk} f_{wx}^k)^2 + 2C(\sum_{k=0}^{n} P_{wxak} f_{wx}^k)(\sum_{k=0}^{n} P_{wxbk} f_{wx}^k)]. \quad \text{A. 1}$$

Expanding all of the terms of A. (1) results in

$$G(f_{wx}) = \varepsilon_x^2\{A\sum_{i=0}^{n}[P_{wxai}(\sum_{j=0}^{n} P_{wxaj} f_{wx}^{i+j})] + B\sum_{i=0}^{n}[P_{wxbi}(\sum_{j=0}^{n} P_{wxbj} f_{wx}^{i+j})] + 2C\sum_{i=0}^{n}[P_{wxai}(\sum_{j=0}^{n} P_{wxbj} f_{wx}^{i+j})]\}. \quad \text{A. 2}$$

Reorganizing the third term (omitting 2C) of A. (2) in terms of the f_{wx} power (i+j) results in

$$
\begin{aligned}
\sum_{i=0}^{n}[P_{\mathrm{wxa}i}(\sum_{j=0}^{n}P_{\mathrm{wxb}j}f_{\mathrm{wx}}^{i+j})] = {} & P_{\mathrm{wxa}0}P_{\mathrm{wxb}0}f_{\mathrm{wx}}^{0} \\
& + P_{\mathrm{wxa}0}P_{\mathrm{wxb}1}f_{\mathrm{wx}}^{1} + P_{\mathrm{wxa}1}P_{\mathrm{wxb}0}f_{\mathrm{wx}}^{1} \\
& \cdots \\
& + P_{\mathrm{wxa}0}P_{\mathrm{wxb}n}f_{\mathrm{wx}}^{n} + P_{\mathrm{wxa}1}P_{\mathrm{wxb}(n-1)}f_{\mathrm{wx}}^{n} + \cdots + P_{\mathrm{wxa}n}P_{\mathrm{wxb}0}f_{\mathrm{wx}}^{n} \\
& + P_{\mathrm{wxa}1}P_{\mathrm{wxb}n}f_{\mathrm{wx}}^{n+1} + P_{\mathrm{wxa}2}P_{\mathrm{wxb}(n-1)}f_{\mathrm{wx}}^{n+1} + \cdots + P_{\mathrm{wxa}n}P_{\mathrm{wxb}1}f_{\mathrm{wx}}^{n+1} \\
& \cdots \\
& + P_{\mathrm{wxa}(n-1)}P_{\mathrm{wxb}n}f_{\mathrm{wx}}^{2n-1} + P_{\mathrm{wxa}n}P_{\mathrm{wxb}(n-1)}f_{\mathrm{wx}}^{2n-1} \\
& + P_{\mathrm{wxa}n}P_{\mathrm{wxb}n}f_{\mathrm{wx}}^{2n} \\
= {} & \sum_{k=0}^{n}[f_{\mathrm{wx}}^{k}\sum_{i=0}^{k}P_{\mathrm{wxa}i}P_{\mathrm{wxb}(k-i)}] + \sum_{k=n+1}^{2n}[f_{\mathrm{wx}}^{k}\sum_{i=k-n}^{n}P_{\mathrm{wxa}i}P_{\mathrm{wxb}(k-i)}]
\end{aligned}
\quad \text{A. 3}
$$

The sum functions in the square brackets on the right-hand side of A. (3) correspond to the third expression of Eq. (20). Using the third expression of Eq. (20), the third term of A. (2) is rewritten as follows,

$$
\begin{aligned}
2C\sum_{i=0}^{n}[P_{\mathrm{wxa}i}(\sum_{j=0}^{n}P_{\mathrm{wxb}j}f_{\mathrm{wx}}^{i+j})] = {} & 2C\{\sum_{k=0}^{n}[f_{\mathrm{wx}}^{k}\sum_{i=0}^{k}P_{\mathrm{wxa}i}P_{\mathrm{wxb}(k-i)}] + \sum_{k=n+1}^{2n}[f_{\mathrm{wx}}^{k}\sum_{i=k-n}^{n}P_{\mathrm{wxa}i}P_{\mathrm{wxb}(k-i)}]\} \\
= {} & 2C\sum_{k=0}^{2n}P_{\mathrm{Cx}k}f_{\mathrm{wx}}^{k}
\end{aligned}
\quad , \quad \text{A. 4}
$$

where P_{Cxk} has the same meaning as in Eq. (20). Similarly, we can rewrite the other two terms in A. (2) as follows:

$$
\begin{aligned}
A\sum_{i=0}^{n}[P_{\mathrm{wxa}i}(\sum_{j=0}^{n}P_{\mathrm{wxa}j}f_{\mathrm{wx}}^{i+j})] &= A\{\sum_{k=0}^{n}[f_{\mathrm{wx}}^{k}\sum_{i=0}^{k}P_{\mathrm{wxa}i}P_{\mathrm{wxa}(k-i)}] + \sum_{k=n+1}^{2n}[f_{\mathrm{wx}}^{k}\sum_{i=k-n}^{n}P_{\mathrm{wxa}i}P_{\mathrm{wxa}(k-i)}]\} = A\sum_{k=0}^{2n}P_{\mathrm{Ax}k}f_{\mathrm{wx}}^{k} \\
B\sum_{i=0}^{n}[P_{\mathrm{wxb}i}(\sum_{j=0}^{n}P_{\mathrm{wxb}j}f_{\mathrm{wx}}^{i+j})] &= B\{\sum_{k=0}^{n}[f_{\mathrm{wx}}^{k}\sum_{i=0}^{k}P_{\mathrm{wxb}i}P_{\mathrm{wxb}(k-i)}] + \sum_{k=n+1}^{2n}[f_{\mathrm{wx}}^{k}\sum_{i=k-n}^{n}P_{\mathrm{wxb}i}P_{\mathrm{wxb}(k-i)}]\} = B\sum_{k=0}^{2n}P_{\mathrm{Bx}k}f_{\mathrm{wx}}^{k}
\end{aligned}
\quad . \quad \text{A. 5}
$$

Because these three expressions (A. (4) and A. (5)) contain the same sum function with respect to k from 0 to $2n$, A. (2) can be rewritten as follows:

$$
\begin{aligned}
G(f_{\mathrm{wx}}) &= \varepsilon_{\mathrm{x}}^{2}(A\sum_{k=0}^{2n}P_{\mathrm{Ax}k}f_{\mathrm{wx}}^{k} + B\sum_{k=0}^{2n}P_{\mathrm{Bx}k}f_{\mathrm{wx}}^{k} + 2C\sum_{k=0}^{2n}P_{\mathrm{Cx}k}f_{\mathrm{wx}}^{k}) \\
&= \varepsilon_{\mathrm{x}}^{2}\sum_{k=0}^{2n}(AP_{\mathrm{Ax}k}f_{\mathrm{wx}}^{k} + BP_{\mathrm{Bx}k}f_{\mathrm{wx}}^{k} + 2CP_{\mathrm{Cx}k}f_{\mathrm{wx}}^{k}) \\
&= \varepsilon_{\mathrm{x}}^{2}\sum_{k=0}^{2n}(AP_{\mathrm{Ax}k} + BP_{\mathrm{Bx}k} + 2CP_{\mathrm{Cx}k})f_{\mathrm{wx}}^{k} \\
&= \varepsilon_{\mathrm{x}}^{2}\sum_{k=0}^{2n}P_{\mathrm{x}k}f_{\mathrm{wx}}^{k}
\end{aligned}
\quad . \quad \text{A. 6}
$$

References

Aydin, K. and Seliga, T. A.: Radar Polarimetric Backscattering Properties of Conical Graupel, *J. Atmos. Sci*., 41, 1887-1892, 1984.

Barker, D., Huang, X. Y., Liu, Z., Auligné, T., Zhang, X., Rugg, S., et al.: The Weather Research and Forecasting (WRF) Model"s Community Variational/Ensemble Data Assimilation System: WRFDA. *Bull. Amer. Meteor. Soc.*, 93, 831-843, 2012.

Borderies, M., Caumont, O., Augros, C., Bresson, É., Delanoë, J., Ducrocq, V., Fourrié, N., Bastard, T. L., and Nuret, M.: Simulation of W - band radar reflectivity for model validation and data assimilation, Quart. J. Roy. Meteorol. Soc., 144, 391-403, 2018.

Caumont, O., Ducrocq, V., Delrieu, G., Gosset, M., Pinty, J.-P., Parent du Châtelet, J., Andrieu, H., Lemaître, Y., and Scialom, G.: A radar simulator for high-resolution nonhydrostatic models, J. Atmos. Oceanic Technol., 23, 1049-1067, 2006.

Caumont, O., Ducrocq, V., Wattrelot, É., Jaubert, G., and Pradier-Vabre, S.: 1D+ 3DVar assimilation of radar reflectivity data: A proof of concept, Tellus A: Dynamic Meteorology and Oceanography, 62, 173-187, 2010.

Dawson, D. T., Ii, Xue, M., Milbrandt, J. A., and Yau, M. K.: Comparison of Evaporation and Cold Pool Development between Single-Moment and Multimoment Bulk Microphysics Schemes in Idealized Simulations of Tornadic Thunderstorms, Mon. Wea. Rev., 138, 1152-1171, 2010.

Evensen, G.: The ensemble Kalman filter: Theoretical formulation and practical implementation, Ocean dynamics, 53, 343-367, 2003.

Gao, J. and Stensrud, D. J.: Assimilation of reflectivity data in a convective-scale, cycled 3DVAR framework with hydrometeor classification, J. Atmos. Sci., 69, 1054-1065, 2012.

Hu, M., Xue, M., Gao, J., and Brewster, K.: 3DVAR and cloud analysis with WSR-88D level-II data for the prediction of the Fort Worth, Texas, tornadic thunderstorms. Part II: Impact of radial velocity analysis via 3DVAR, Mon. Wea. Rev., 134, 699-721, 2006.

Jung, Y., Xue, M., and Zhang, G.: Simulations of polarimetric radar signatures of a supercell storm using a two-moment bulk microphysics scheme, J. Appl. Meteor. Climatol., 49, 146-163, 2010.

Jung, Y., Zhang, G., and Xue, M.: Assimilation of simulated polarimetric radar data for a convective storm using the ensemble Kalman filter. Part I: Observation operators for reflectivity and polarimetric variables, Mon. Wea. Rev., 136, 2228-2245, ~~2008~~2008a.

Jung, Y., Xue, M., Zhang, G., and Straka, J. M.: Assimilation of simulated polarimetric radar data for a convective storm using the ensemble Kalman filter. Part II: Impact of polarimetric data on storm analysis, Mon. Wea. Rev., 136, 2246-2260, 2008b.

Kawabata, T., Schwitalla, T., Adachi, A., Bauer, H.-S., Wulfmeyer, V., Nagumo, N., and Yamauchi, H.: Observational operators for dual polarimetric radars in variational data assimilation systems (PolRad VAR v1. 0), Geoscientific Model Development, 11, 2493-2501, 2018.

Liu, C., Xue, M., and Kong, R.: Direct Assimilation of Radar Reflectivity Data using 3DVAR: Treatment of Hydrometeor Background Errors and OSSE Tests, Mon. Wea. Rev., 2018. 2018.

Pfeifer, M., Craig, G., Hagen, M., and Keil, C.: A polarimetric radar forward operator for model evaluation, J. Appl. Meteor. Climatol., 47, 3202-3220, 2008.

Posselt, D. J., Li, X., Tushaus, S. A., and Mecikalski, J. R.: Assimilation of dual-polarization radar observations in mixed-and ice-phase regions of convective storms: Information content and forward model errors, Mon. Wea. Rev., 143, 2611-2636, 2015.

Putnam, B. J., Xue, M., Jung, Y., Snook, N., and Zhang, G.: The Analysis and Prediction of Microphysical States and Polarimetric Radar Variables in a Mesoscale Convective System Using Double-Moment Microphysics, Multinetwork Radar Data, and the Ensemble Kalman Filter, Mon. Wea. Rev., 142, 141-162, 2014.

Ryzhkov, A., Pinsky, M., Pokrovsky, A., and Khain, A.: Polarimetric radar observation operator for a cloud model with spectral microphysics, J. Appl. Meteor. Climatol., 50, 873-894, 2011.

Schwitalla, T. and Wulfmeyer, V.: Radar data assimilation experiments using the IPM WRF Rapid Update Cycle, Meteorologische Zeitschrift, 23, 79-102, 2018.

Snook, N., Xue, M., and Jung, Y.: Analysis of a Tornadic Mesoscale Convective Vortex Based on Ensemble Kalman Filter Assimilation of CASA X-Band and WSR-88D Radar Data, Mon. Wea. Rev., 139, 3446-3468, 2011.

Snook, N., Xue, M., and Jung, Y.: Ensemble Probabilistic Forecasts of a Tornadic Mesoscale Convective System from Ensemble Kalman Filter Analyses Using WSR-88D and CASA Radar Data, Mon. Wea. Rev., 140, 2126-2146, 2012.

Snook, N., Xue, M., and Jung, Y.: Multiscale EnKF Assimilation of Radar and Conventional Observations and Ensemble Forecasting for a Tornadic Mesoscale Convective System, Mon. Wea. Rev., 143, 1035-1057, 2015.

Sun, J. and Crook, N. A.: Dynamical and microphysical retrieval from Doppler radar observations using a cloud model and its adjoint. Part I: Model development and simulated data experiments, J. Atmos. Sci., 54, 1642-1661, 1997.

Sun, J. and Wang, H.: Radar data assimilation with WRF 4D-Var. Part II: Comparison with 3D-Var for a squall line over the US Great Plains, Mon. Wea. Rev., 141, 2245-2264, 2013.

Tong, M. and Xue, M.: Ensemble Kalman Filter Assimilation of Doppler Radar Data with a Compressible Nonhydrostatic Model: OSS Experiments, Mon. Wea. Rev., 133, 1789-1807, 2005.

Wang, H., Sun, J., Fan, S., and Huang, X.-Y.: Indirect assimilation of radar reflectivity with WRF 3D-Var and its impact on prediction of four summertime convective events, J. Appl. Meteor. Climatol., 52, 889-902, 2013a.

Wang, H., Sun, J., Zhang, X., Huang, X.-Y., and Auligné, T.: Radar data assimilation with WRF 4D-Var. Part I: System development and preliminary testing, Mon. Wea. Rev., 141, 2224-2244, 2013b.

Wang, Y. and Wang, X.: Direct assimilation of radar reflectivity without tangent linear and adjoint of the nonlinear observation operator in the GSI-based EnVar system: Methodology and experiment with the 8 May 2003 Oklahoma City tornadic supercell, Mon. Wea. Rev., 145, 1447-1471, 2017.

Wattrelot, E., Caumont, O., and Mahfouf, J.-F.: Operational implementation of the 1D+ 3D-Var assimilation method of radar reflectivity data in the AROME model, Mon. Wea. Rev., 142, 1852-1873, 2014.

Xiao, Q., Kuo, Y.-H., Sun, J., Lee, W.-C., Barker, D. M., and Lim, E.: An approach of radar reflectivity data assimilation and its assessment with the inland QPF of Typhoon Rusa (2002) at landfall, J. Appl. Meteor. Climatol., 46, 14-22, 2007.

Xue, M., Tong, M., and Droegemeier, K. K.: An OSSE framework based on the ensemble square root Kalman filter for evaluating the impact of data from radar networks on thunderstorm analysis and forecasting, J. Atmos. Oceanic Technol., 23, 46-66, 2006.

Zhang, G., Vivekanandan, J., and Brandes, E.: A method for estimating rain rate and drop size distribution from polarimetric radar measurements, IEEE Transactions on Geoscience and Remote Sensing, 39, 830-841, 2001.

Tables

Table 1 Values of α_{dsa}, α_{dsb}, α_{dga}, and α_{dgb}.

α_{dsa}	α_{dsb}	α_{dga}	α_{dgb}
0.194×10^{-4}	0.191×10^{-4}	$0.\sout{191}105\times10^{-3}$	$0.\sout{165}092\times10^{-3}$

Table 2 Values of P_{wxak} and P_{wxbk} in Eq. (16).

k	0	1	2	3	4	5	6
P_{wsak}	0.194	7.094	2.135	-5.225	0	0	0
P_{wsbk}	0.191	6.916	-2.841	-1.160	0	0	0
P_{wgak}	0.~~191~~105	~~2.39~~1.821	- ~~12.57~~3.765	~~38.71~~- 0.797	- ~~65.53~~16.28	~~56.16~~- 21.97	- ~~18.988~~.744
P_{wgbk}	0.~~165~~092	1.~~72~~929	-9.~~92~~794	~~32.15~~29.24	-~~56.0~~48.19	~~48.84~~39.34	- ~~16.69~~12.20

Table 3 Perturbation samples for the verification of the tangent linear operator.

	q_r (kg kg^{-1})	q_s (kg kg^{-1})	q_g (kg kg^{-1})	ratio
sample 1	min: -4.1×10^{-4} max: 4.7×10^{-4}	min: -4.2×10^{-4} max: 4.4×10^{-4}	min: -3.7×10^{-4} max: 3.1×10^{-4}	1.00114799
sample 2	min: -1.6×10^{-6} max: 1.8×10^{-6}	min: -1.6×10^{-6} max: 1.7×10^{-6}	min: -1.4×10^{-6} max: 1.2×10^{-6}	1.00004709

Figures

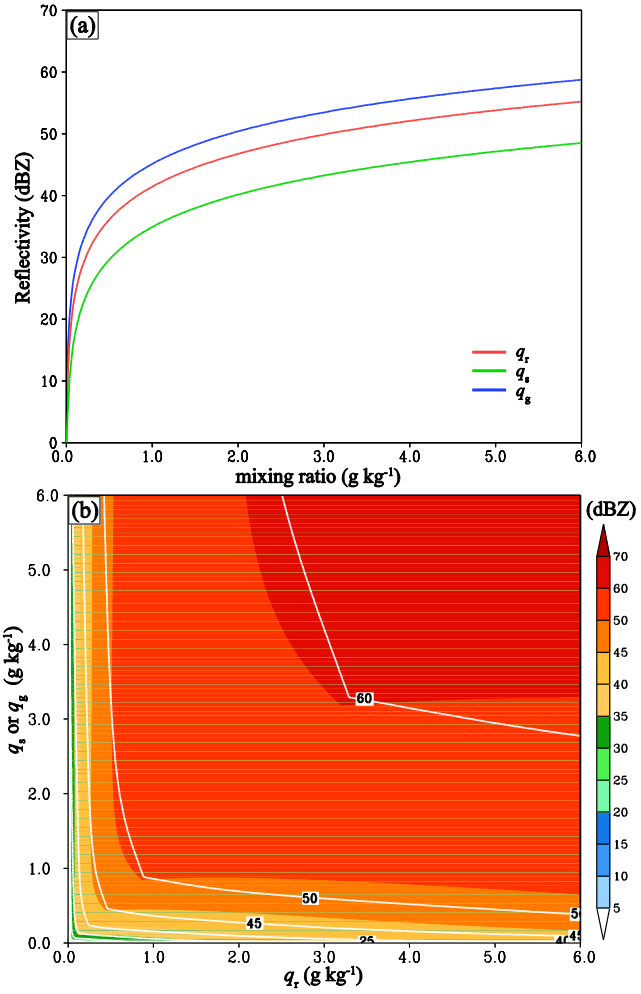

Fig. 1 (a) The reflectivity as (a) a function of q_r (red), q_s (green), and q_g (blue) for pure water and dry snow/graupel and (b) a function of q_r–q_s (colors) and q_r–q_g (contours) for wet snow/graupel.

5

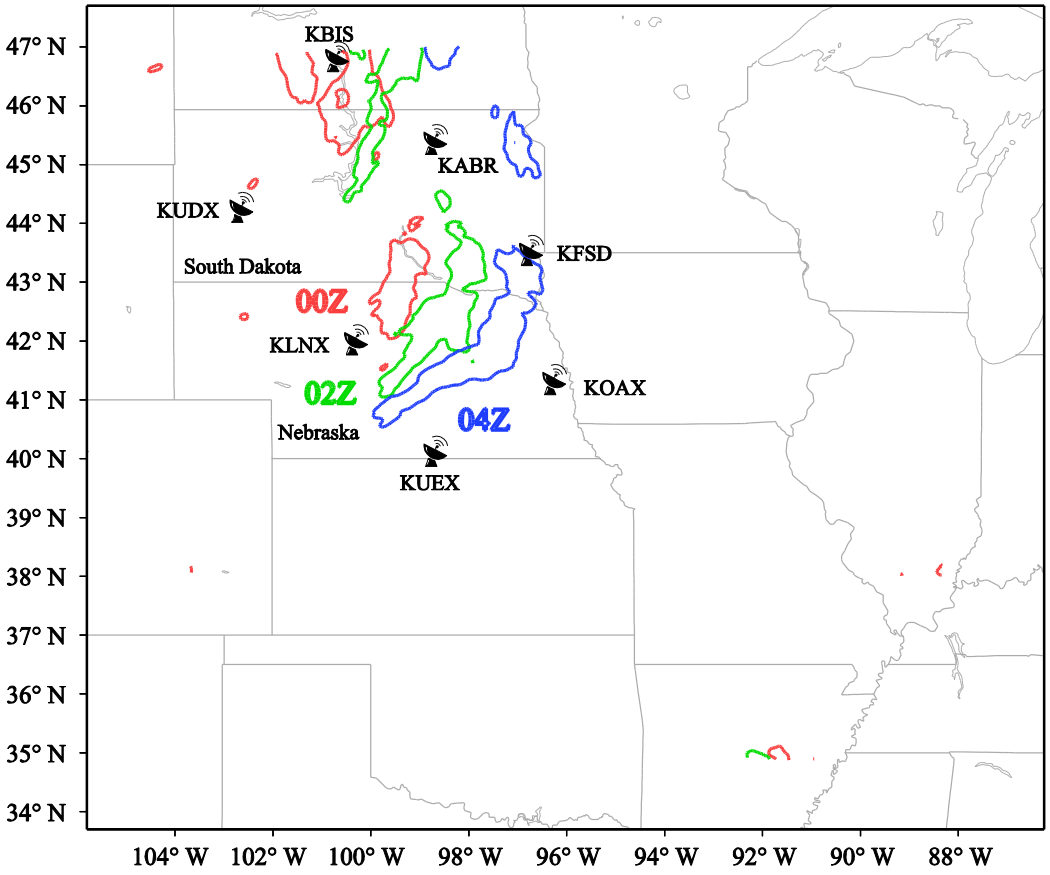

Fig. 2 The simulation domain with radar sites marked by radar icons and names. The areas of precipitation greater than 5 mm h^{-1} are plotted for 00Z (red), 02Z (green), and 04Z (blue) on 2 June 2018.

5

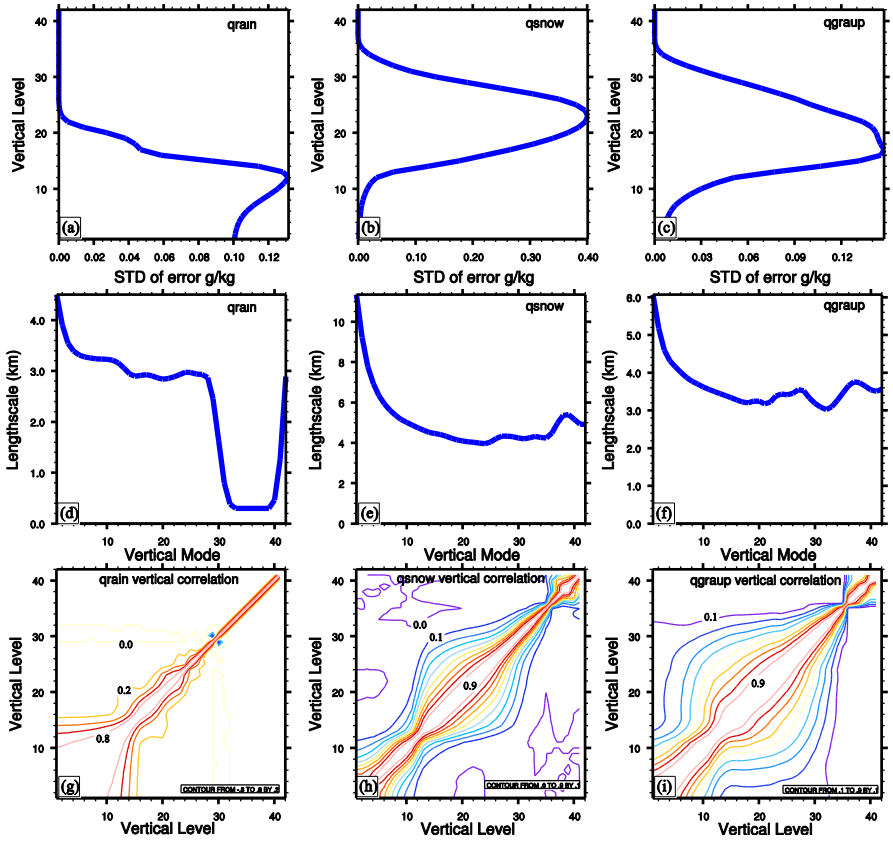

Fig. 3 (a-c) The standard deviations of the background errors at different vertical levels, (d-f) the horizontal correlation length scale as a function of EOF mode, and (g-i) the vertical correlation coefficients for q_r, q_s, and q_g.

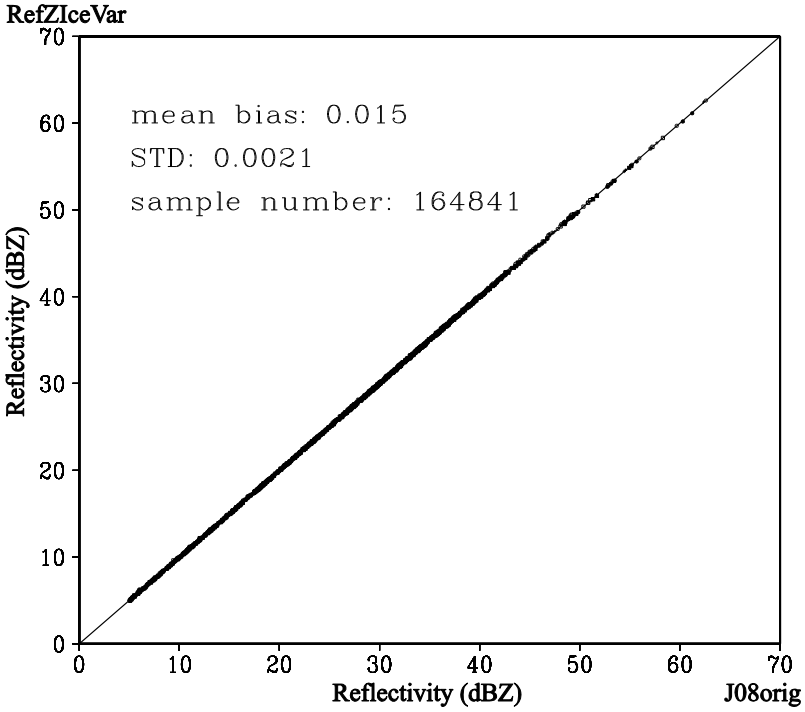

Fig. 4 Scatter plot of the reflectivity for J08orig (*x* axis) versus RadarVar (*y* axis). The bias, standard deviation (STD), and number of samples are listed in the plot.

5

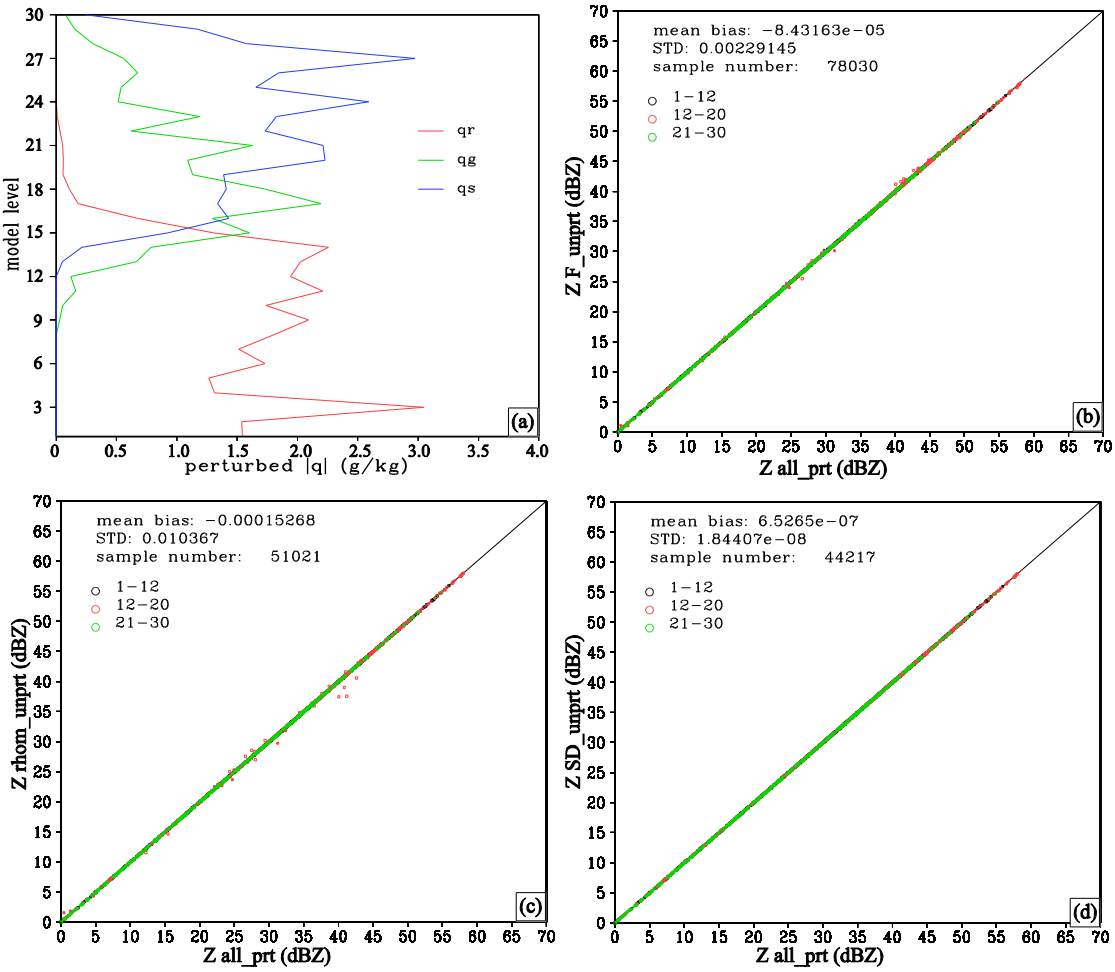

Fig. 5 (a) Vertical distributions of the maximum absolute values of the perturbed q_r (red), q_s (green), and q_g (blue). Reflectivity scatter plots of all_prt (x axis) versus (b) F_unprt (y axis), (c) rhom_unprt (y axis), and (d) SD_unprt (y axis) at model levels 1~12 (black, lower than 3 km AGL), 12~20 (red, between 3~7 km AGL), and 21~30 (green, above 7 km AGL).

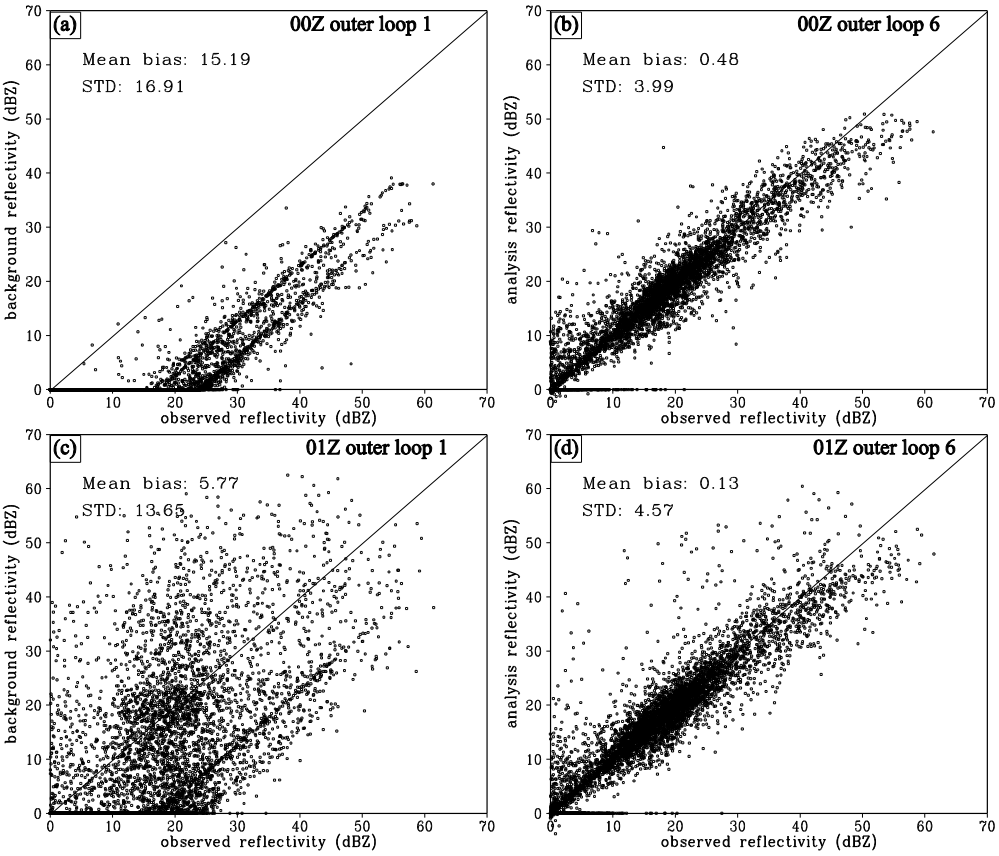

Fig. 6 Scatter plots of the observed (*x* axis) versus (a, c) background and (b, d) analysis reflectivity at (a, b) 00Z and (c, d) 01Z in Exp_ref. The mean bias and standard deviation (STD) between the observations and the background (or analysis) are listed in each plot.

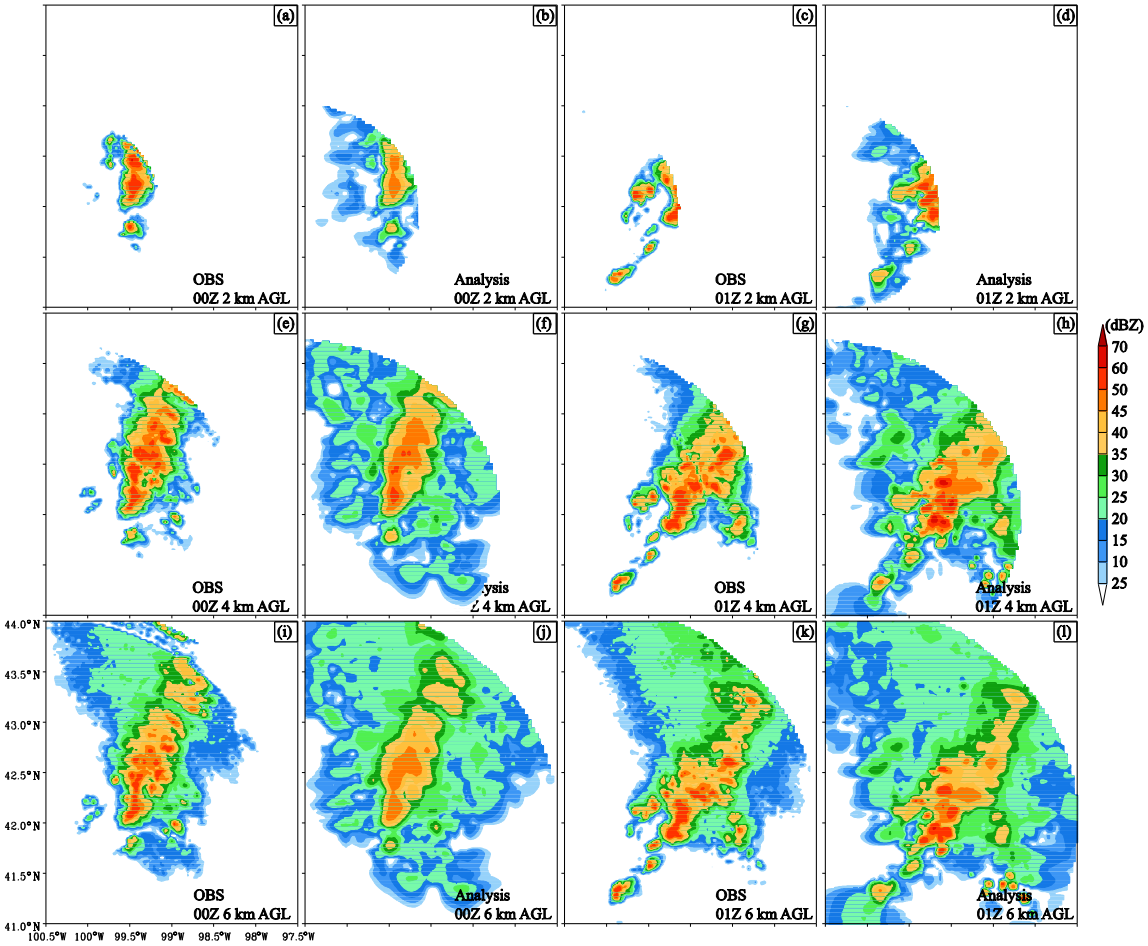

Fig. 7 The (a, e, i, c, g, k) observed (KLNX) and (b, f, j, d, h, l) analysis reflectivities at (a-d) 2 km, (e-h) 4 km, and (i-l) 6 km AGL at (a, e, i, b, f, j) 00Z and (c, g, k, d, h, l) 01Z in Exp_ref.

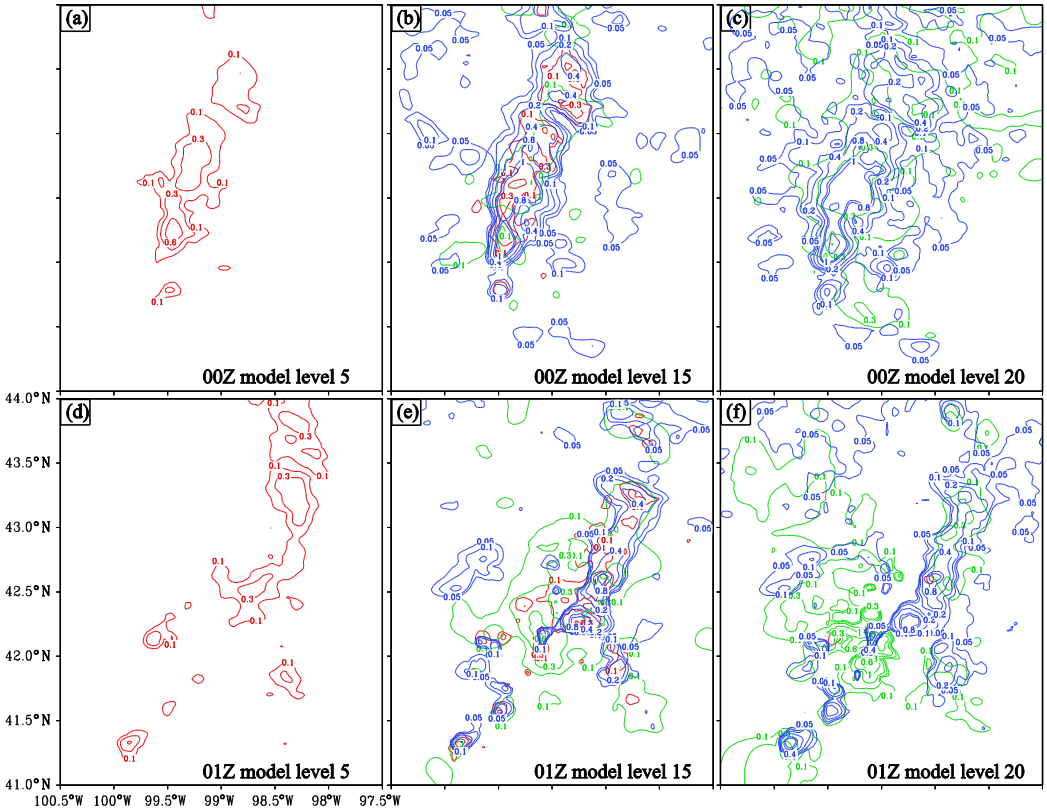

Fig. 8 The (a, b, c) 00Z and (d, e, f) 01Z analyses of q_r (red), q_s (green), and q_g (blue) at model levels 5 (left column), 15 (middle column), and 20 (right column) for outer loop 6 in Exp_ref. Model levels 5, 15, and 20 approximately correspond to 0.7 km, 4.0 km, and 8.0 km AGL, respectively.

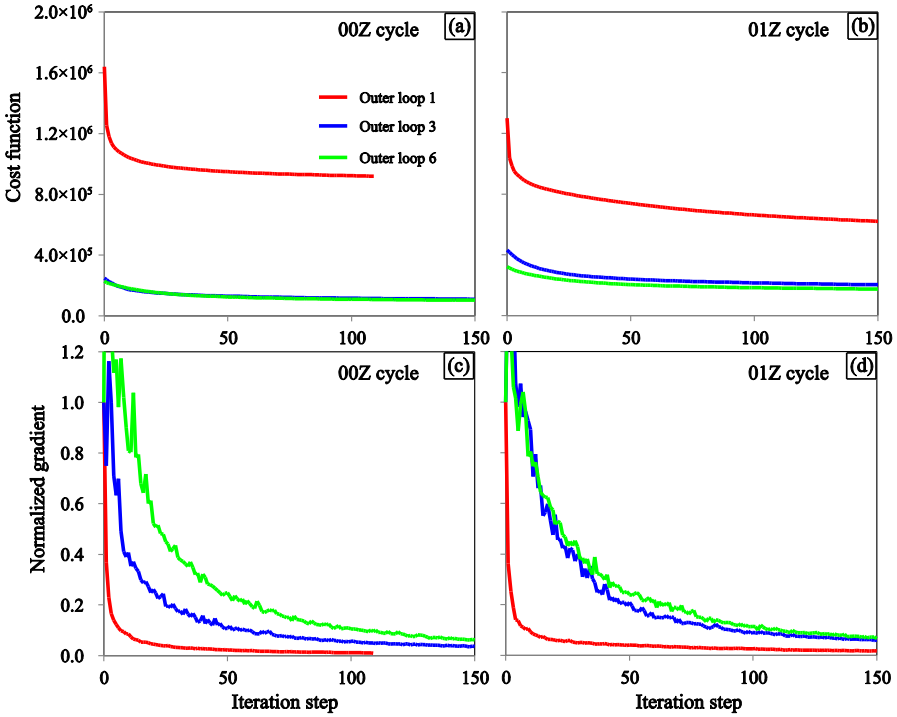

Fig. 9 The cost function and normalized gradient norm as functions of the iteration step during the minimization at (a, c) 00Z and (b, d) 01Z in Exp_ref.

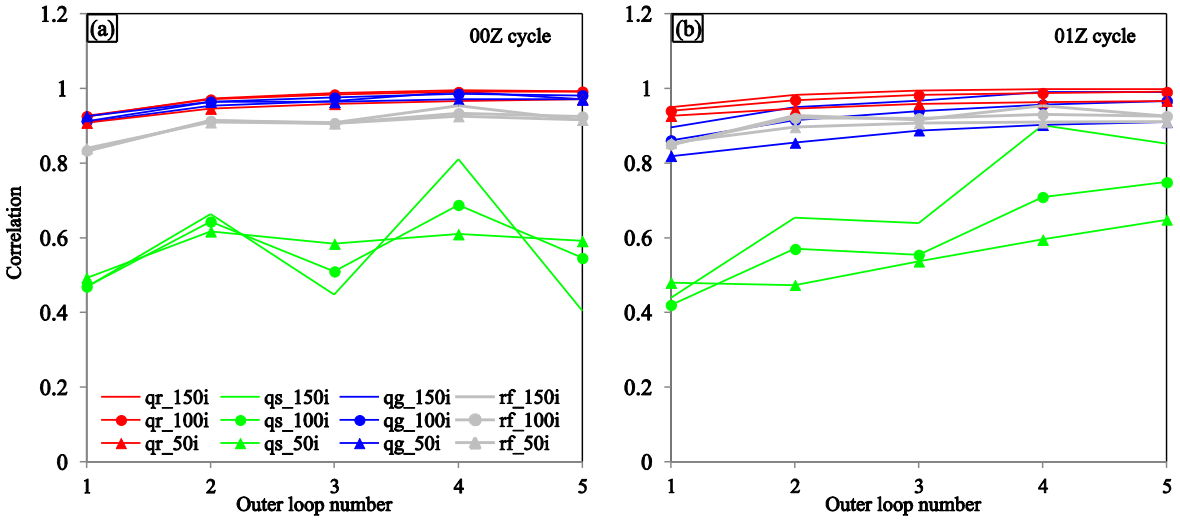

Fig. 10 The correlation coefficients of q_r (red), q_s (green), q_g (blue), and reflectivity (gray) between the Exp_ref analysis (with six outer loops and 150 inner iterations each loop) and that with different numbers of outer loops and inner iterations at (a) 00Z and (b) 01Z.

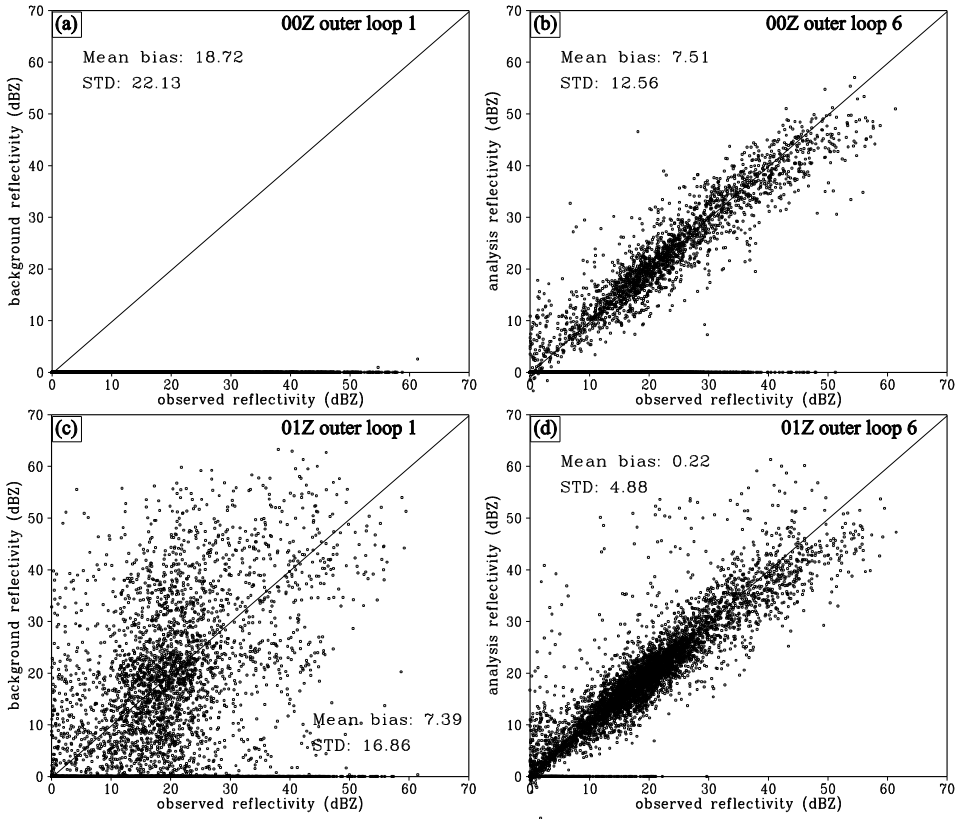

Fig. 11 Same as Fig. 6 but for the experiments without hydrometeor preprocessing at (a, b) 00Z and (c, d) 01Z.

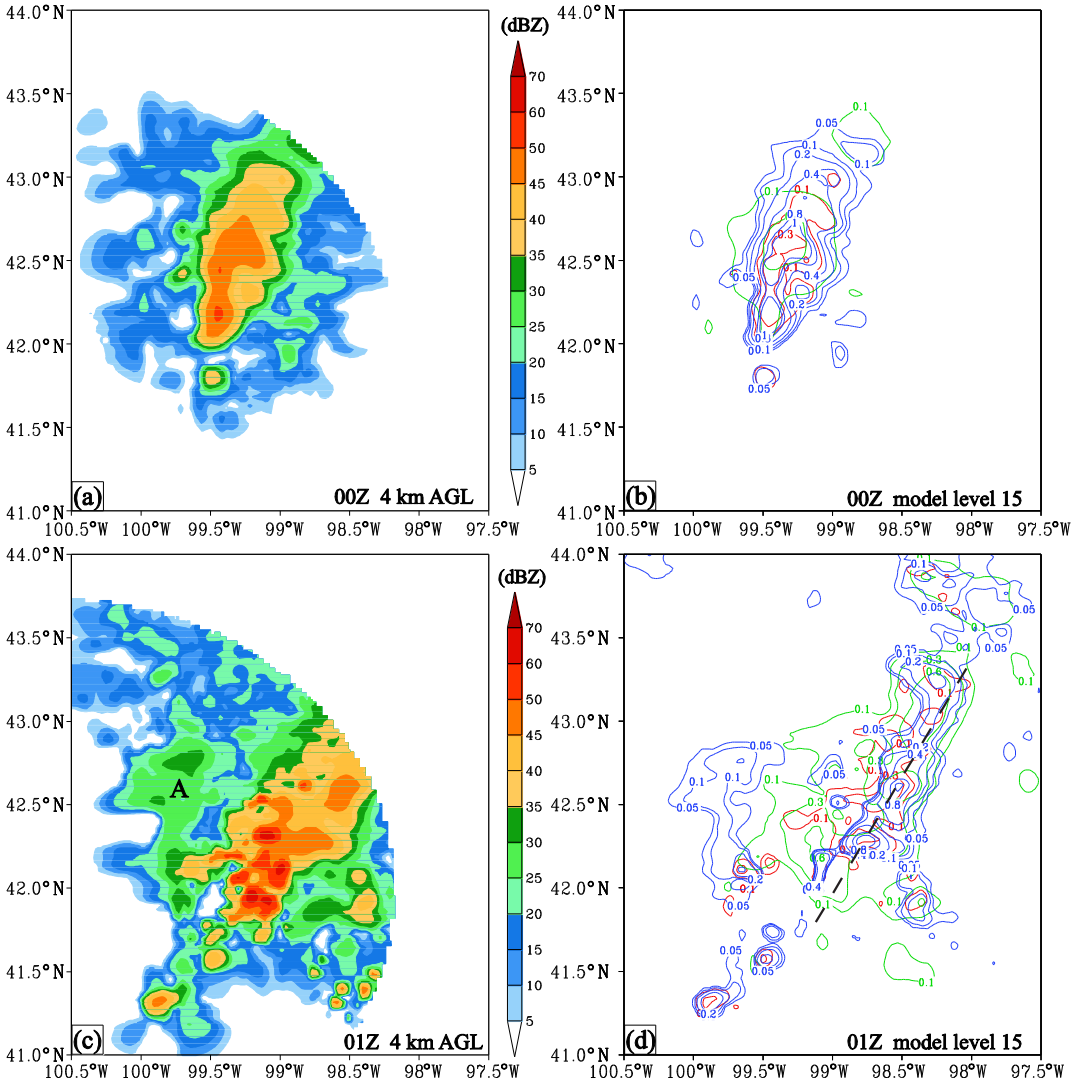

Fig. 12 (a, c) The analysis reflectivity at 4 km AGL and (b, d) the analyses of q_r (red), q_s (green), and q_g (blue) at model level 15 at 00Z and 01Z for the experiments without hydrometeor preprocessing.

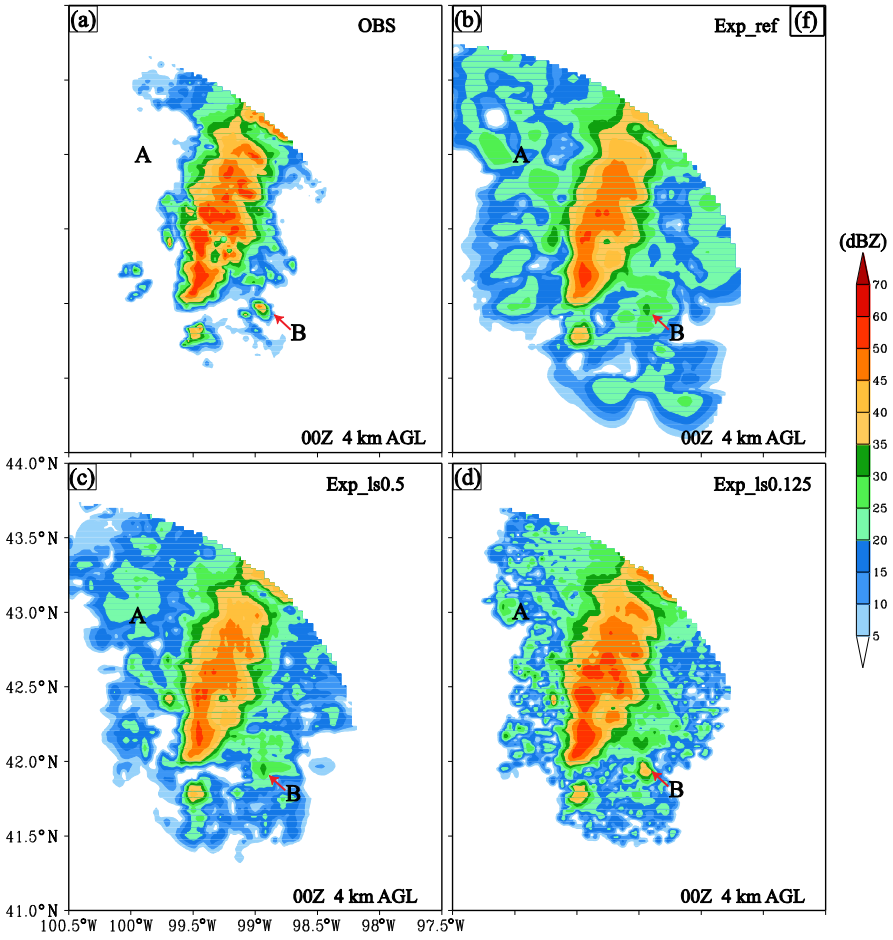

Fig. 13 Same as Fig. 7 but for (a) the observations and the analyses from (b) Exp_ref, (c) Exp_ls0.5, and (d) Exp_ls0.125.

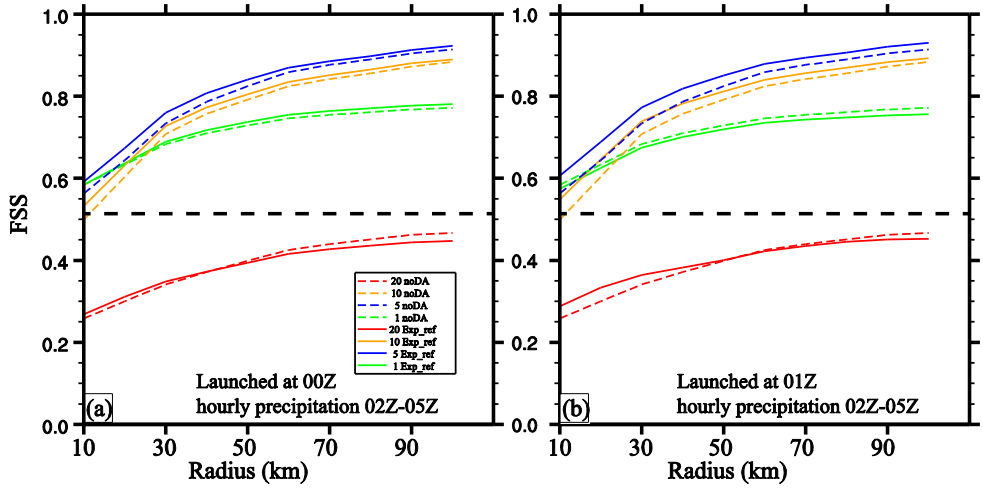

Fig. 14 The FSSs of the hourly precipitation forecasts aggregated over the period from 02Z to 05Z as functions of the radius of influence for forecasts launched from the (a) 00Z and (b) 01Z analyses for Exp_ref (solid lines) and noDA (dashed lines). The hourly precipitation thresholds are denoted by green (1 mm h^{-1}), blue (5 mm h^{-1}), orange (10 mm h^{-1}), and red (20 mm h^{-1}) lines. The dashed straight line represents the skillful FSS at 1 mm h^{-1}.